The Precipitation Life Cycle of Mesoscale Convective Complexes over the Central United States

RAY L. MCANELLY AND WILLIAM R. COTTON

Colorado State University, Department of Atmospheric Science, Fort Collins, Colorado

ABSTRACT

The mesoscale convective complex (MCC) is a common and particularly well-organized class of meso-α-scale storm systems over the central United States. As observed by infrared (IR) satellite, the typical MCC's 10–12 h evolution displays a fairly consistent sequence of events, including the monotonic areal expansion of its anvil from its formation to its maximum size, followed by the monotonic shrinkage of the colder cloud top areas as the system weakens and dissipates. Primarily within the growth phase of this cycle, a characteristic IR signature reflects the MCC in its most intense, mesoconvective stage, which lasts ~4 h and during which the coldest cloud top area reaches its largest extent.

Hourly precipitation data have been analyzed for 122 MCC cases that were selected from June–August 1977–83 and screened to insure a reasonable conformity with the typical IR life cycle. On average, these systems produced a rainfall volume of 3.46 km^3 during their life cycle, over an area of 3.20×10^5 km^2 and at an average depth of 10.8 mm. Relative to a normalized, IR-defined life cycle, the averaged trends of hourly rainfall area, intensity, and volume all have well-defined growth/decay cycles, but with significantly staggered maxima. Average rainfall intensity (R), and the proportion of measurable reports due to convective intensities, attain maxima early in the life cycle. Hourly rainfall volumes (V) are more symmetrically distributed in time, with the maximum occurring near the largest anvil size (based on $-54°$C IR threshold). Active rainfall area (A) continues to increase until ~1 h after maximum anvil size. The IR-defined, intense mesoconvective stage corresponds to that portion of the life cycle from maximum R to maximum A, and is so termed because of the large areal extent and volumetric rate of convective precipitation intensities. A large area of stratiform precipitation is generated during this stage; it persists and becomes increasingly dominant as convective activity subsides during the latter stages of the life cycle. Averaged mappings of the precipitation data show that throughout the MCC life cycle, the heaviest rainfall tends to be displaced 50–100 km south of the cloud-shield centroid, while the stratiform pattern tends to be more MCC-centered.

A statistical analysis of these precipitation characteristics, derived individually for each case, provides an estimate of the natural interstorm variability for typical summertime MCCs. A comparison of various composite subsets of the sample reveals several interesting tendencies: 1) smaller, less-organized systems tended to be "drier" than similar-sized but better-organized MCCs; 2) large systems were "rainier" than smaller ones through much of the life cycle, not only in terms of A and V, as expected, but also in terms of R; 3) large systems tended to be "rainier" in the eastern part of the sample domain than in the western part, but this was not so for small systems; and 4) the eastern systems, both large and small, had a more coherent and intense core of heavy precipitation through their life cycle than the western systems.

1. Introduction

The mesoscale convective complex (MCC) has been identified by Maddox (1980) as a common and distinct class of predominantly nocturnal, meso-α-scale (200–2000 km, >6 h) storm systems over the central United States. The infrared (IR) satellite-defined criteria chosen for MCCs (Table 1a) effectively isolate them toward the larger end of the size spectrum for mesoscale convective systems (MCSs) in general, and indicate a particularly extensive region of mid- to upper-tropospheric

upward mass flux (Maddox 1983) that is convectively driven (Fritsch and Maddox 1981) and accompanied by a widespread area of stratiform precipitation. Mesoscale convective complexes impact a number of forecasting problems in and downstream of this region, but are probably most significant in terms of their abundant rainfall. Fritsch et al. (1986), in a study of 74 MCCs from 1982 and 1983, concluded that MCCs typically account for 20–50% of annual rainfall over a broad region of the Central Plains states, with June–August precipitation being particularly dominated by MCCs.

Case studies of MCCs (or closely related events) indicate that there is an extreme case-to-case variability in internal substructure and evolution. Cases described by Smull and Houze (1985), Leary and Rappaport

Corresponding author address: Mr. Ray L. McAnelly, Colorado State University, Dept. of Atmospheric Science, Fort Collins, CO 80523.

TABLE 1. Definitions of MCCs based on MB-enhanced IR satellite imagery.

(a) From Maddox (1980)		(b) Current study	
Parameter	Definition	Parameter	Definition
Size	A—Cloud shield with continuously low IR temperature $\leqslant -32°C$ must have an area $\geqslant 100\,000$ km² B—Interior cold cloud region with temperature $\leqslant -52°C$ must have an area $\geqslant 50\,000$ km²	Size	Contiguous cloud shield with IR temperature $< -54°C$ must have area $\geqslant 50\,000$ km²
Duration	Size definitions A and B must be met for a period $\geqslant 6$ h	Duration	Size definition must be met for a period $\geqslant 6$ h
Shape	Eccentricity (minor axis/major axis) $\geqslant 0.7$ at time of maximum extent	Shape	Minor-to-major axis ratio of $-54°C$ area $\geqslant 0.7$ at maximum size
Initiate	Size definitions A and B are first satisfied	Start	Size definition is first satisfied
Maximum extent	Contiguous cold cloud shield (IR temperature $\leqslant -32°C$) reaches maximum size	Maximum	Contiguous cloud shield area colder than $-54°C$ reaches maximum size
Terminate	Size definitions A and B no longer satisfied	End	Size definition no longer satisfied

(1987), and Rutledge et al. (1988) were dominated by a single mesoscale line of intense convection, behind which developed an extensive trailing region of stratiform precipitation. Such quasi-two-dimensional structure is similar to the generalized view of squall-type tropical cloud clusters (Zipser 1977; Houze 1977). More complex in substructure and evolution were cases discussed by McAnelly and Cotton (1986), Maddox et al. (1986), Watson et al. (1988), Rockwood et al. (1984), and Fortune and McAnelly (1986). In general, these cases were characterized not by a single substructural convective component, but instead by multiple meso-β-scale (<200 km, <6 h) convective components that together produced the MCC. One or more of these convective components would dominate the overall system for awhile until another component (or other components) intensified and became dominant. In these cases, too, a widespread area of stratiform precipitation developed beneath the cloud shield.

Some of the case-to-case substructural variability in MCC-type events has been related to several characteristic synoptic settings (Clark et al. 1980; Merritt and Fritsch, 1984; Blanchard and Watson, 1986). Even within the quasi-steady synoptic pattern during the 8-day MCC episode discussed by McAnelly and Cotton (1986), slight day-to-day synoptic changes and environmental modifications by previous MCS activity appeared to be partly responsible for producing different substructures in the various MCCs.

Despite the substructural variability seen by McAnelly and Cotton (1986) in the episode's MCCs, the bulk precipitation characteristics of the systems evolved in a consistent manner relative to their IR-defined life cycle. Kane et al.'s (1987; hereafter referred to as KCF) precipitation analysis of the same 74 MCCs studied by Fritsch et al. (1986), also imply that various synoptic groupings of MCC events are all characterized by similar life cycles. Thus, regardless of the synoptic setting and internal structure of MCCs, satellite and precipitation data exhibit a generalized, consistent life cycle that reflects a meso-α-scale organization. Such a life cycle appears to be similar to that described by Leary (1984) and generalized by Zipser (1982) for mesoscale precipitation features in the tropical Atlantic.

In this paper, a composite precipitation analysis methodology similar to that used by McAnelly and Cotton (1986) is extended to a sample consisting of 122 MCCs that occurred in June–August, in order to establish more reliably the precipitation life cycle of the average summertime MCC and to examine its case-to-case variability. This precipitation analysis is similar in many respects to that described by KCF, but differs in both approach and objectives in two major ways: (1) while KCF utilized a large number of 24-h precipitation reports to define in detail the total precipitation patterns in their MCC cases, we use a far fewer number of 1-h reports and emphasize the temporal evolution of precipitation in ours; (2) KCF utilized a larger space–time domain in defining their total-case precipitation fields. For instance, they included all of the initial thunderstorms and meso-β-scale clusters that might eventually merge into the mature system. In contrast, our space–time domains are more conservatively restricted to the mature meso-α-scale system, with the emphasis being on the evolution of the primary system.

2. Data and analysis methodology

Only two data sources were used in this study: Geostationary Operational Environmental Satellite (GOES) imagery, and United States hourly precipitation data. The satellite-defined tracks in Fig. 1 show
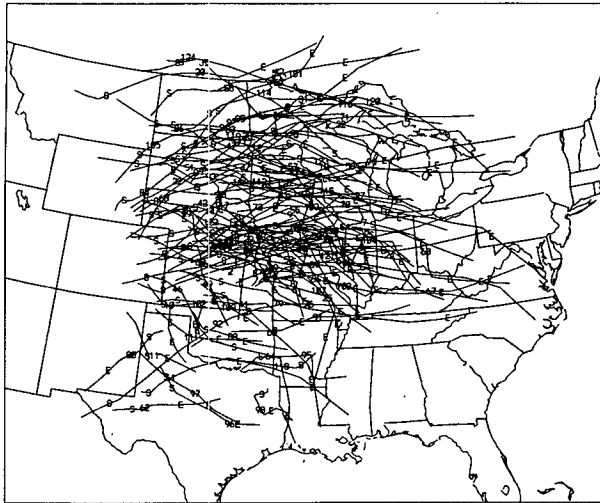
SYSTEM TRACKS

FULL MCC SAMPLE
122 SYSTEMS

FIG. 1. Satellite-defined tracks of the 122 MCCs in the analysis sample, based on centroids of the cloud-shield area colder than −54°C at 3-h intervals. Each MCC track extends from 3.75 h before its *start* position (*S*) to 3.75 h after its *end* position (*E*), with the *maximum* position given by the system number.
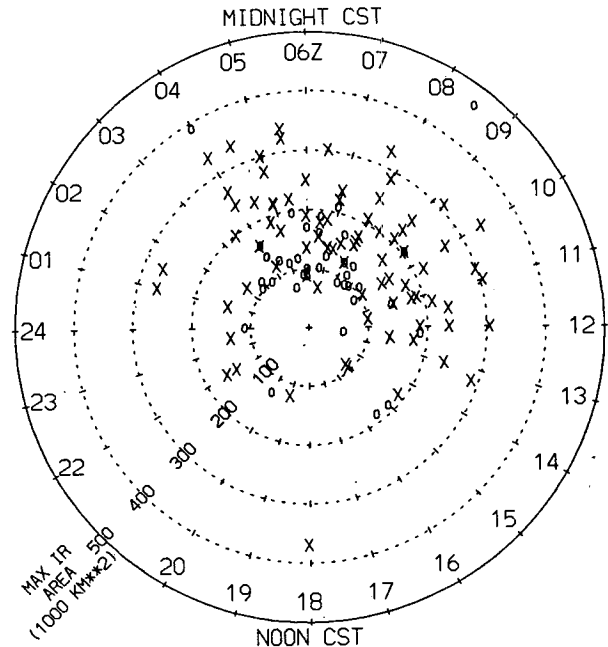

FIG. 2. Distributions of diurnal timing (UTC clock coordinate; 0600 UTC = 0000 central standard time) and size (radial coordinate) of the 122 MCCs at their maximum −54°C areal extent. Large ×'s denote the relatively better organized and more 'ideal' systems with ratings 5–9 (see text), and small ○'s denote the lower-rated systems (ratings 1–4). Time averages in text are based on maximum-size times from −0300 to 2100 UTC.

the geographical distribution of the 122 cases, and Fig. 2 shows their timing and size distributions at maximum IR extent. The hourly precipitation network is shown in Fig. 3. In short, satellite imagery was used to define an objective, normalized life cycle for each MCC, in which ten subperiods of similar duration are defined that span the entire growth/decay cycle. Hourly precipitation data were then objectively analyzed for each case within the context of its normalized life cycle, yielding several precipitation variables for each subperiod, and for the total storm period. These individual-case analyses were then averaged or composited over various groupings of cases. Figure 4 summarizes the relation between the normalized life cycle; the composite, IR-observed cloud-shield evolution for the 122-case sample; and the storm-centered circular areas over which the bulk precipitation variables were derived. The space and time dependency of the circular areas are illustrated for the average MCC track in Fig. 5. A more detailed description of the analysis methodology follows.

a. Satellite data

Our objective in case selection was to identify a set of MCCs that conformed reasonably well to the single growth/decay cloud-shield cycle illustrated in Fig. 4, so that the normalized life cycle could be applied consistently to each case. First of all, our sample is restricted to the summertime months of June, July and August; cases occurring earlier or later in the convective season
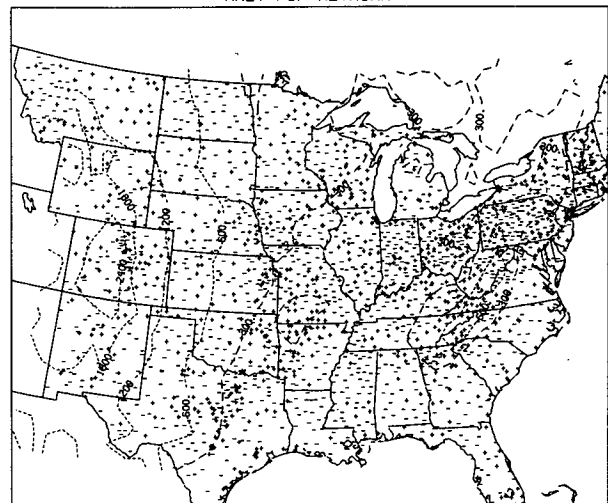

FIG. 3. Hourly precipitation network. Plusses and minuses denote gages with resolution of 0.25 and 2.5 mm, respectively. Only operable stations for a given MCC event near the middle of the 7-yr sample are shown. Other MCCs in the sample would show slightly different station/gage configurations, due to station closings, openings, and location and gage-type changes, and a different set of missing-data stations. Terrain is contoured (m).
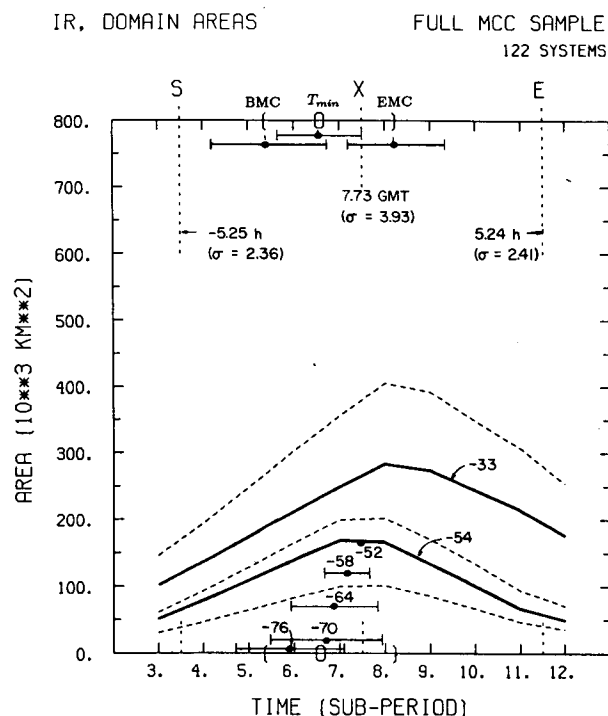
IR. DOMAIN AREAS   FULL MCC SAMPLE
                              122 SYSTEMS

FIG. 4. Idealized growth trends of IR areas colder than −54° and −33°C (solid curves), averaged over the 122 MCC cases, relative to normalized life cycle. The *maximum* time (X) and *start* (S)-*to-maximum* and *maximum-to-end* (E) durations define each system's normalized life cycle and subperiods 3–12. The averages and standard deviations (σ) of these times are indicated. The timing (and $\pm\sigma$ bars) for three subjectively defined IR features (see text) are also indicated: the beginning and end of an intense *mesoconvective stage* (parentheses labelled BMC and EMC), and a *mesoscale thermal minimum* (the 'O' labelled T_{min}). The average timing (and $\pm\sigma$) and size of several maximum areas, as thresholded by the indicated colder IR temperatures, were derived from a sample of 19 MCCs from June 1985. The −76°C area is the average of the only 10 of the 19 that reached temperatures that cold. Dashed curves show composite circular areas of three MCC-centered, concentric domains used for the bulk precipitation analysis.

were eliminated in an attempt to screen out those which may have had relatively large baroclinic influences. Further screening was accomplished through an examination of routine GOES satellite imagery, where the candidate cases were primarily those tabulated for 1978–83 in the series of seasonal MCC summaries that was begun by Maddox (1980) and continued by NOAA/ERL's Weather Research Program (WRP; e.g., Rodgers et al., 1985).[1] Of the 147 June–August MCCs listed in these summaries, 113 (77%) were considered to be "typical" and were retained in our sample. Nine

[1] Unpublished summaries for 1979 and 1980 were available from Maddox (1981) and Rodgers (personal communication), respectively. An episode of MCCs in August 1977, tabulated by Wetzel et al. (1983), was also considered.
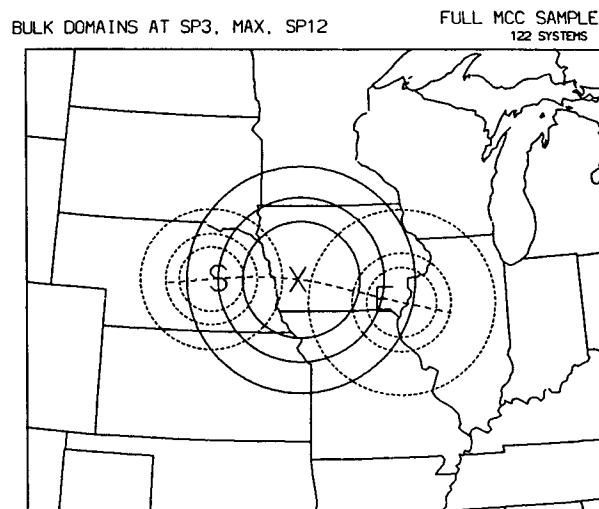
BULK DOMAINS AT SP3. MAX. SP12   FULL MCC SAMPLE
                                            122 SYSTEMS

FIG. 5. Average track (dashed line) of 122-case composite MCC over subperiods 1–14. Here S, X and E denote centroid of −54°C area at the *start, maximum* and *end,* respectively. The three domain areas from Fig. 4 are shown for subperiods 3 and 12 (dotted circles) and at the MCC *maximum* (solid circles).

more cases that were not tabulated in the summaries were added to give a total analysis sample of 122 cases.

The cases not retained were rejected for a variety of reasons. For example, cases were omitted if they occurred beyond the data domain (e.g., entirely in Canada) or if they matured too far from our central United States focal point (e.g., along the Atlantic or Gulf coasts). Some cases were rejected because they apparently never became well organized, or because they displayed an atypical evolution that made it difficult to assign the normalized life cycle. These include systems involved in a complex merger or split with another MCS, having a double growth/decay cycle not conforming to the single cycle in Fig. 4, or having a width/ length ratio < 0.7 for extended portions of their life cycle. By rejecting these atypical cases, we have avoided some of the analysis problems discussed by KCF. Finally, there was insufficient satellite imagery (in the archive we used at WRP) to define or assess the lifecycles of some of the cases; these were primarily typical cases highlighted in the annual summaries, so they represent missed opportunities for analysis.

The satellite-defined life cycle assigned to each MCC is based on the contiguous cloud shield area with IR radiances colder than −54°C. A *mature* MCC is defined to *start* when the −54°C area first exceeds 50 000 km², to reach its *maximum* when this region attains its largest areal extent, and to *end* when the −54°C area first becomes less than 50 000 km² (Table 1b). These definitions, which are based on easily identifiable areas in "MB-enhanced" imagery (Clark 1983), are slightly modified from those specified in Table 1a, which involve a warmer IR threshold of −33°C as well as

$-54°C.^2$ This simplification is justified on two counts: 1) although the $-54°C$ contour usually encloses an area unambiguously associated with a given MCC, the larger $-33°C$ area is often contiguous with cloud shields of other MCSs (Augustine and Howard 1988) or may be an undifferentiated part of a larger-scale cloud pattern (e.g., a "comma" cloud) within which the MCC is embedded; thus, a boundary determination (and areal measurements) based on the warmer threshold is more subjective[3]; 2) most of an MCC's precipitating area is confined within the colder threshold, while the warmer, surrounding cloud shield is mostly nonprecipitating (McAnelly and Cotton 1986). However, the maximum $-33°C$ area of each MCC also was measured for use in the precipitation analysis, as discussed later.

In addition to these primary life-cycle benchmarks, an IR-defined *mesoconvective stage*, so termed a posteriori based on the precipitation analysis, has been determined for each case. It is this characteristic IR signature that identifies the MCC as an intense, highly organized meso-α-scale system in the imagery (e.g., Figs. 6–7), and is subjectively determined by a relatively smooth and circular $-54°C$ contour, and by a relatively strong and uniform IR thermal gradient around the outer portions of the enhanced cloud shield. This stage begins during the MCC's growth, typically after the merged cloud-shield lobes associated with two or more initial meso-β-scale convective clusters lose their individual identities as they consolidate into a unified, near-circular meso-α-scale cloud shield. The signature usually persists for several hours, until the $-54°C$ contour becomes ragged as the cloud shield warms and/or begins to fragment. Usually occurring within the *mesoconvective stage*, a mesoscale *thermal minimum* was determined as the time at which the central region of colder cloud tops (lighter shading colder than the $-60°$ to $-63°C$ black region; see Fig.

6) reaches its largest and coldest extent.[4] The qualifier "mesoscale" implies that it is not determined by the coldest pixel or overshooting top, but by a subjective, thermally-weighted integration of the colder pixels over a widespread area. While determining the *mesoconvective stage* and *thermal minimum* was quite subjective and difficult in some cases, objective techniques (using digital imagery) could be devised to identify these features in most cases.

These life-cycle points were temporally defined for each MCC by examining MB-enhanced imagery at intervals of usually 15 or 30 min, and rarely longer than 1 h. Fourteen subperiods of the normalized life-cycle are defined relative to the primary IR benchmarks, such that the *start-to-maximum* duration of each case is divided into the four equal subperiods 4–7, and the *maximum-to-end* duration is equally divided into subperiods 8–11. Subperiods 1–3 and 12–14 are comprised of 1.5-h periods before and after the MCC's *mature* status. Most of our analysis is confined to the ten subperiods 3–12.

Figure 4 illustrates the average timing of the IR features for the 122-case composite in terms of the normalized life cycle. The average *start-to-maximum* and *maximum-to-end* durations are both a little over 5 h, such that each of the eight subperiods 4–11 lasts 1.3 h. The $-54°C$ area for each subperiod in Fig. 4 is an average over the 122 cases, each of which is assumed to grow linearly in area from 50 000 km^2 at subperiod 3 to its measured size at its *maximum*, then to decay linearly to 50 000 km^2 at the *end* time. Similarly, the $-33°C$ area is prescribed to grow from 100 000 km^2 to its maximum size, which is assumed to occur 1 h after the $-54°C$ *maximum*, then to decay to $\frac{2}{3}$ its maximum size at the *end*. The 1-h lag of the $-33°C$ maximum and its $\frac{2}{3}$-maximum ending size are assumptions based on the 12-case study of McAnelly and Cotton (1986). It should be stressed that IR areal measurements were not made except to define the *start*, *maximum*, and *end* times, and that the idealized IR growth/decay pattern was used only to provide a consistent framework for analyzing each MCC's precipitation data.

Also entered on Fig. 4 are the average size and normalized timing of several IR areal maxima, as defined by thresholds ranging from $-52°$ to $-76°C$, that were available for 19 MCCs that occurred in June 1985 (Augustine and Howard 1988; Augustine, personal communication). The later-occurring maxima of areas defined by successively warmer thresholds is consistent with the later-occurring $-33°C$ maximum. It is also consistent with the average mesoscale *thermal minimum* occurring prior to the MCC *maximum*, which was evident in McAnelly and Cotton's (1986) study

---

[2] The description of the MB enhancement curve by Clark (1983) indicates a $2.0°C$ discrepancy in the IR temperatures corresponding to the threshold count values for several of the repeat gray shades and those labeled on the sample MB image therein, which has been reproduced widely by Maddox (1980) and elsewhere. Technical personnel from NOAA/NESDIS have confirmed that the current thresholds are as indicated above the 1977 gray-scale bar in Fig. 6, which is consistent in scaling with these thresholds. Thus, the two thresholds in question, $-33.2°$ and $-54.2°C$, were apparently constant over the 7-yr study period; they are referred to as $-33°$ and $-54°C$ in this paper. Earlier MCC definitions (which use $-32°C$ and either $-52°$ or $-53°C$) that are based on MB imagery, as well as numerous mislabeled MB images in the literature, are apparently in error by $1°–2°C$. These discrepancies probably arose from operational changes in the MB curve or calibration changes in the IR sensors during the mid-1970s (Scofield, personal communication).

[3] The revised, automated method currently used by NOAA/ERL's Weather Research Program in their seasonal MCC compilations has also abandoned use of the warmer threshold (Augustine 1985; Augustine and Howard 1988). Note that their use of the $-52°C$ threshold with digital imagery should result in slight biases relative to MCC statistics based on the $-54°C$ area in MB-enhanced imagery.

[4] The subjective, IR-defined *mesoconvective stage* and *thermal minimum* are the same features as identified by McAnelly and Cotton (1986), but have been renamed more accurately.
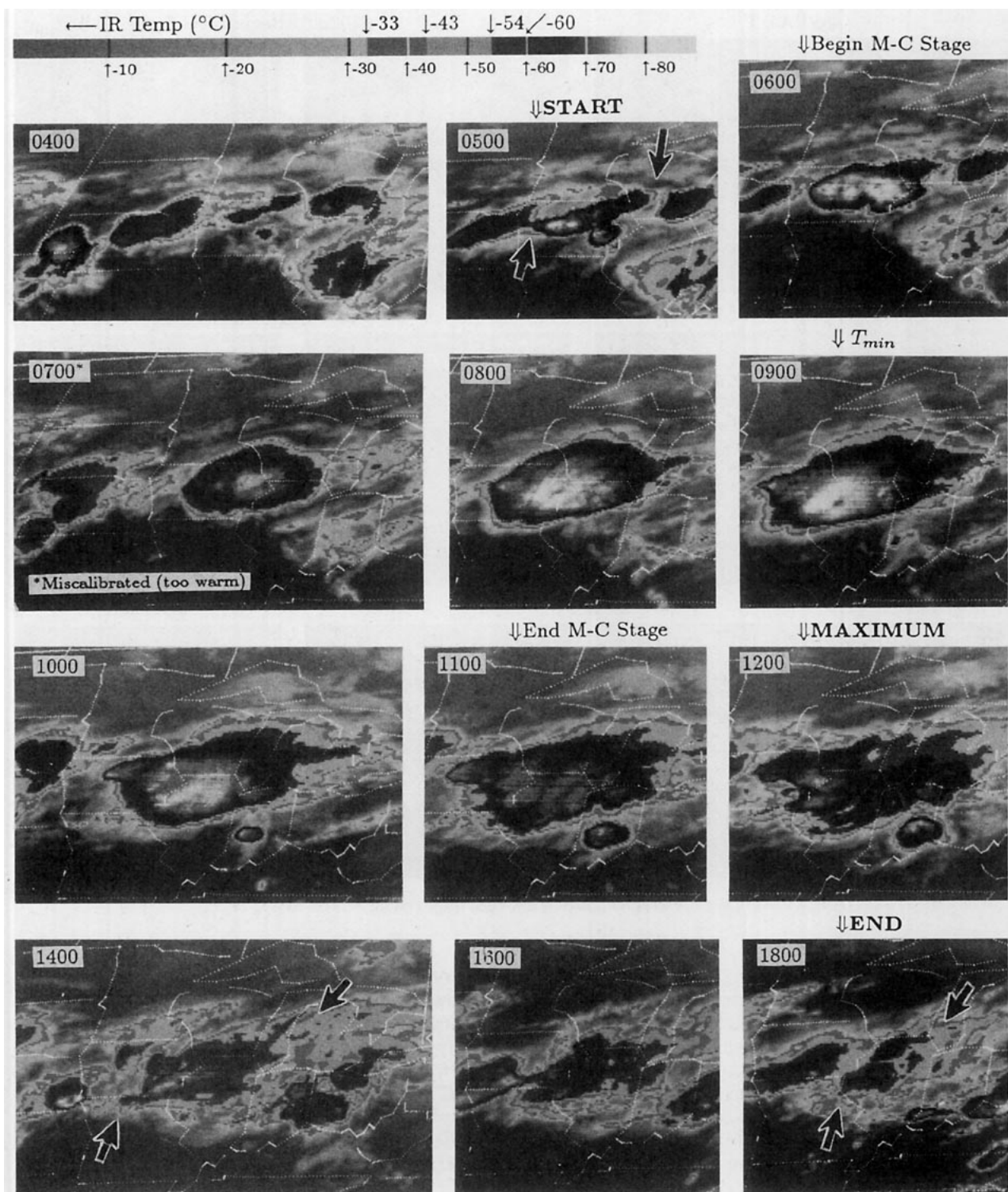
FIG. 6. The MB-enhanced, IR satellite sequence showing the evolution of a relatively high-rated MCC (rating = 7; see text) on 8 Aug 1977. Indicated times are UTC. *Start, maximum* and *end* times are indicated, as are the beginning and ending of the *mesoconvective (M-C) stage* and the *mesoscale thermal minimum* (T_{min}). Each pair of arrows (at selected times) indicates the long-axis ends of the −54°C (dark-contoured) cloud-shield area considered to be the MCC. The temperature scaling for the MB enhancement is indicated (°C) below the gray-scale bar; the values above the bar indicate IR thresholds (°C, with 0.2 decimal omitted) for the contours associated with discrete gray-scale steps.
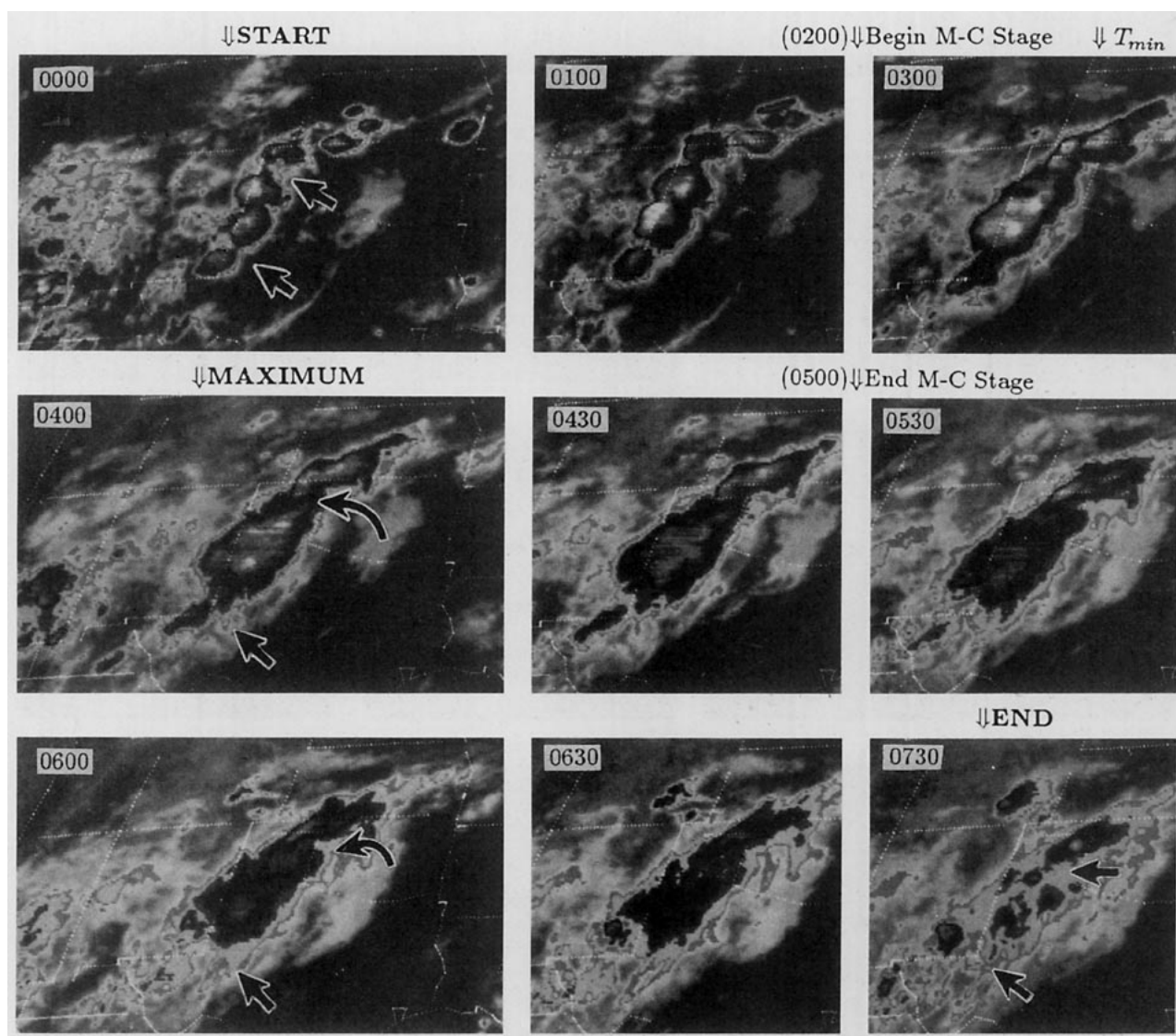
FIG. 7. As in Fig. 6, except for relatively low-rated MCC (rating = 2) on 10 Aug 1977.

as well as in this larger sample. The average *mesoconvective stage* in Fig. 4, which lasts 3.8 h, encompasses this typical smaller-to-larger succession of maximum areas as defined by colder-to-warmer thresholds.

In addition to defining each MCC's temporal life cycle, the satellite imagery was used to define storm tracks, based on 3-h positions of the −54°C centroid (Fig. 1). Finally, an overall subjective rating was assigned to each system based on its satellite evolution. Ratings ranged from 1 for relatively poorly organized, elongated MCCs with a marginally-defined *mesoconvective stage* and/or with significant amounts of nearby "contaminating" convection that was not part of the system, to 9 for the "perfect", isolated, near-circular MCC with an intense, well-defined *mesoconvective stage*. An MCC highlighted by Maddox (1980; his Fig. 7) is one such perfect case in our sample. Figures 6–7

show typical examples of systems with relatively high and low ratings of 7 and 2, respectively. The only detrimental aspects to the system in Fig. 6 are nearby MCS activity near the beginning and end of the life cycle, and a fragmentation of a large (eastern) portion of the −54°C area at 1200 UTC away from the primary system by 1400 UTC. The system in Fig. 7 was rated low because of the contiguous MCS appendages on its southern and (especially) northern flanks throughout the life cycle, but was retained in the sample because of an otherwise typical evolution (including its *mesoconvective stage*) between those appendages. These ratings were made in order to stratify relatively "ideal" MCCs from ones less organized or less isolated, and to compare their composite precipitation characteristics. As seen in Fig. 2, the lower-rated systems tended to be smaller, with maximum −54°C areas < 200 000 km^2.

b. Hourly precipitation data

The hourly precipitation data[5] were recorded by the hydrological network depicted in Fig. 3. While this network has fewer gages by an order of magnitude than the 24-h stations used by KCF, it provides excellent temporal resolution relative to the MCC's 10–12 h life cycle, and adequate spatial resolution to determine its meso-β-scale substructure. The network consists of high-resolution weighing gages, from which hourly accumulations are rounded to the nearest 0.25 mm, and low-resolution tipping-bucket gages, which count the number of accumulations reaching 2.5 mm each hour. Because of the inability of a network of this sparsity to accurately record the highly variable nature of convective rainfall, and because of the relative insensitivity of the 2.5-mm gages to light stratiform rainfall, the recorded rainfall distribution for a given hour of an MCC will contain inaccuracies. However, by averaging the data over a given normalized subperiod and over a large number of cases, such sampling error is reduced, and representative composite precipitation characteristics for that subperiod can be derived. The sampling error associated with this network is discussed in more detail in section 4b.

Two analysis methodologies were taken: a bulk precipitation one which treated the storm system as a whole, and a coarsely gridded mapping analysis.

For each MCC, the bulk precipitation analysis was done for every hour over three concentric, circular domains, and over the period spanning subperiods 3–12. The use of the circular domains provided an effective, consistent, and automated method of objectively analyzing each case without regard to its particular cloud-shield asymmetries. These domains are storm centered, with the center given by the storm position at halfway through the hourly period along the tracks in Fig. 1. Their sizes are time-dependent functions of each system's idealized IR cloud-shield area, as indicated in Fig. 4. The largest circular domain is a factor of 1.43 larger than the $-33°$C area at midway through the hour, such that if this $-33°$C area is an ellipse with a minor-to-major axis ratio of 0.70, it is circumscribed by the domain. This domain was chosen with respect to the shape factor from Table 1. It is designed to include most, if not all, of the precipitation occurring beneath the contiguous, meso-α-scale cloud shield (MCC-related precipitation), at the risk of occasionally including some nearby, non-MCC precipitation. The second domain is similarly prescribed to be larger than the idealized $-54°$C area, by a factor of 1.18 from subperiod 3 to the *maximum,* followed by a time-dependent factor that increases linearly to 1.43 at subperiod 12. This domain would circumscribe an ellipse having

the $-54°$C area, and having an axis ratio of 0.85 for the first half of the life cycle, followed by a linear relaxation of the axis ratio to 0.70. It is designed to contain most of the significant MCC precipitation, and accounts for the more circular $-54°$C area that is typically seen in the growing stages than in the latter life-cycle stages. The third and smallest domain is half the area of the second. Entirely within the $-54°$C cloud shield, it is designed to indicate the extent that MCC precipitation is concentrated in the interior cloud-shield region.

Figure 5 illustrates the space and time dependency of these domains for the average MCC track. Since subperiod 3 begins only 1.5-h before the MCC's *start,* we exclude earlier precipitation from the bulk analysis. In contrast, KCF include all precipitation traced back to the "first storms", which occur, on average, about 6 h prior to the *start* (Rodgers et al. 1985). Similarly, they apparently follow the precipitation pattern in time through its dissipation, which would usually extend well beyond our cutoff at subperiod 12 (ending 1.5 h after the *end*). Thus, our temporal domain is considerably shorter in most cases. Our spatial domain would also be smaller than that used by KCF's method in some cases. For instance, an early subperiod domain, centered on a growing MCC, would not include precipitation from a separate meso-β-scale convective cluster occurring well ahead of the primary system, even if the cluster was eventually overtaken by the main system and a later subperiod domain. Similarly, a large fragment might split off the primary MCC cloud shield and track beyond the largest domain (though we have attempted to minimize such problems with our case selection). Thus, our space–time domain is more conservatively restricted to the primary MCC than KCF's.

Three hourly precipitation variables were derived for each domain, using both gage types as independent samples. This separation of samples was necessary because of their inherent biases on the variables; however, as shown later, the evolution of the variables is consistent between the two samples. First, for each of the three annular regions defined by the concentric domains, the area of measurable precipitation (A) was computed as the ratio of measurable to total number of reports tabulated over the annular region, multiplied by its area (such that the stations received equal weight over the area considered, despite their irregular spacing). Second, the average rain intensity (R) of each measurable area is the arithmetic average of the measurable reports (which were also tabulated into subperiod intensity arrays in order to examine the intensity distribution). Third, the volumetric rain rate was computed as $V = AR$. Hourly values for each of the two larger domains as a whole were then derived for A and V by summing the annular values, and for R by averaging the annular R values, weighted by the corresponding A values. These hourly variables for both gage-type samples were then smoothed temporally with

---

a 1–2–1 running filter, in order to eliminate some of the hour-to-hour variability that is due to inadequate sampling while still retaining adequate meso-β-scale temporal resolution (<6 h). A third, combined-gage sample was created by averaging the smoothed 0.25 and 2.5-mm variables. Finally, the smoothed hourly values were time-averaged over each subperiod, with a given hour weighted by its time spent in a subperiod.

Note from Figs. 1 and 3 that some systems were outside the data network for part of their lifetime; subperiod variables were computed only if ~80% or more of the cloud shield was over the network during that subperiod. Of the 122 MCCs, the number of valid cases per subperiod ranged from 106 to 117. For the 101 cases that spent subperiods 3–12 entirely in the precipitation network, cumulative precipitation volumes (CV) were computed for each domain by multiplying the volumetric rates V by the duration of the subperiods, and sequentially summing the resultant volumes over subperiods 3–12. Thus, CV represents the total rainfall occurring in the space–time swaths of the domains illustrated in Fig. 5.

In summary, the bulk precipitation analysis for each MCC resulted in four variables (A, R, V, CV) for each subperiod 3–12, for each combination of gage-type sample (0.25 mm, 2.5 mm, and combined) and the three domains. These variables were then averaged over various groupings of MCCs to produce the composite bulk analyses. This individual-case derivation of the variables also allowed case-to-case variation to be examined (section 4).

A similar mapped precipitation analysis was applied to all 14 subperiods of each MCC. For each subperiod, a storm-centered cartesian domain was defined such that the x-axis aligned along the storm motion at that time in its life cycle. The 10×10 grid contains square cells with sides of 0.625 deg latitude (69.5 km). Hourly precipitation observations were tabulated into the subperiod containing the midpoint of the hourly period, and into the grid cells according to their relative position to the center. For each cell, subperiod values of precipitating area and volumetric rate (A and V) were computed as described above for both independent gage-type samples, but with no temporal smoothing. Due to sparse station spacing and storm proximity to the network borders, each subperiod analysis grid generally contained a substantial number of grid cells with no hourly observations for one or both gage types; no attempt was made to fill in such cells by interpolation.

Total life-cycle accumulation, defined for a given gage location as the rainfall occurring within the space-time swath of the largest circular domain over subperiods 3–12, was similarly mapped (onto a larger grid) relative to the MCC's *maximum* position and *start-to-end* direction of movement, with both gage types included in a single analysis. These individual-case gridded analyses were then averaged into common grids for composite groupings of MCCs, with a variable number of contributing cases per grid cell. The total-storm accumulation mappings are based on an order of magnitude fewer stations than the 24-h stations utilized by KCF, which they objectively analyzed onto a finer, 50-km mesh. We made no attempt to normalize the size of the precipitation patterns as they did.

3. Full-sample composite precipitation life cycle

a. Bulk precipitation analysis

A comparison of the bulk precipitation characteristics for the 122-case composite MCC, as derived over the largest domain from both 0.25- and 2.5-mm gage-type samples, is presented in Fig. 8. The analyses of these independent samples clearly show the gage-type biases in computing hourly measurable precipitation area (A) and the average rain rate over that area (R). The high-resolution 0.25-mm gages consistently yield a larger A, by a factor of 1.5–1.7, due to a larger proportion of them recording a measurable hourly threshold than the 2.5-mm gages. Conversely, the low-resolution gages give an R that is larger at all subperiods, by a factor of 1.4–1.7, because of the absence of values < 2.5 mm h^{-1} in computing their average. These two biases nearly offset each other in their multiplicative effect on volumetric rate (V), however, so that V values for the two samples are similar (within 15%) throughout the life cycle. If trace observations were available and included in the analysis, A would be larger and R lower than those given by the 0.25-mm gage-type analysis, but V would be relatively unaffected.

Despite the biases evident in Fig. 8, the two samples yield very similar trends for each variable. Both samples show A steadily increasing to their maximum values [8.9 and 5.7 ($\times10^4$) km^2 for the 0.25 and 2.5-mm gage samples, respectively] at subperiod 8, about 1 h after the MCC's *maximum* size, followed by a more gradual decline. Note that the maximum raining area, as derived from the more sensitive 0.25-mm sample, is only 53% of the maximum $-54°$C area in Fig. 4, and 32% of the maximum $-33°$C area. Only towards the end of the life cycle does A for this sample approach the diminishing $-54°$C area, and it remains less than one-third of the $-33°$C area throughout the life cycle. The evolution of V in Fig. 8 shows a fairly symmetric distribution centered near the MCC's *maximum*, with maximum rates of 398 and 381 ($\times10^{-3}$) km^3 h^{-1} for the two samples.[6] The trends of R for both samples reach their maxima (5.4 and 7.9 mm h^{-1}) relatively early in the life cycle, and are well into the decay phase before the MCC's *maximum*. Goodman and Mac-Gorman (1986) found that the average timing of peak

---

[6] Each 100 units on the volumetric rate scale in Fig. 8, or 0.1 km^3 h^{-1}, is equivalent to 10^{11} kg h^{-1}, 8.1×10^4 acre-feet h^{-1}, 10 mm h^{-1} over an area of 10^4 km^2 (~1 deg lat–lon), or 1 mm h^{-1} over 10^5 km^2 (about half the area of the typical Plains state).

PCP AREA, RATE, VOL   FULL MCC SAMPLE
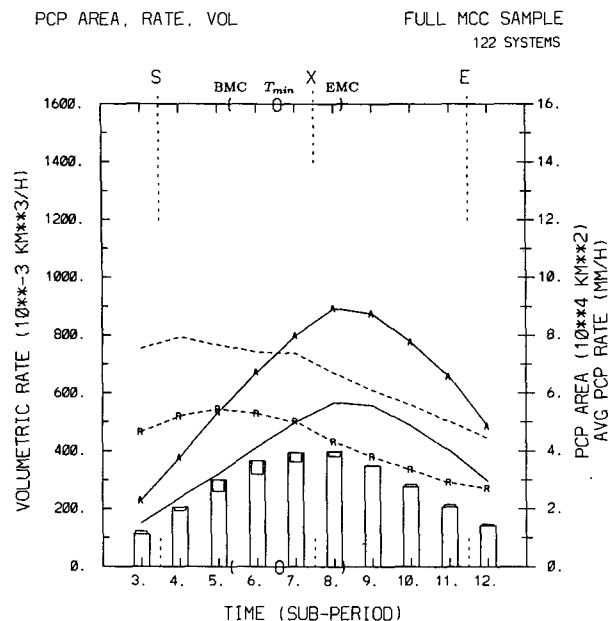   122 SYSTEMS

FIG. 8. Bulk precipitation characteristics for 122-case composite MCC over large domain, as derived from both gage-type samples. Precipitating area (A, solid), average rain intensity (R, dashed) and volumetric rain rate (V, bars) are shown. Primary curves (labeled A and R, wide bars) show 0.25-mm gage analysis. Analysis for 2.5-mm gage sample is shown by unlabeled A and R curves, and by the thinner departure V bars from primary bars. Average IR-defined life cycle is indicated along top and bottom axes as in Fig. 4.

tions which lead to the average rate curves in Figs. 8 and 9 is provided in Fig. 10, which shows the relative distribution of measurable rain reports in the largest domain over several intensity categories for both gage-type samples. These analyses show that the large values of R seen early in the life cycle are due to the maximum relative occurrence of more intense hourly reports, perhaps best delineated by the 7.6-mm h^{-1} threshold. Both samples, especially the more sensitive 0.25-mm gage sample, show that after subperiod 5 or 6, and still during the steady growth stage of the raining area, a shift occurs in the relative contribution of these more intense rates toward lighter intensities. This shift from a relatively small, convectively-dominated system to one characterized by a large extent of more stratiform precipitation, may essentially represent the upscale transformation of the developing system to its long-lived, α-scale stage.

The intensity distributions for the two gage-type samples in Fig. 10 also can be expressed in terms of their areal and volumetric-rate distributions as thresholded by various rainfall intensities. These composite distributions were derived first for both samples and then averaged to produce the combined-gage analysis in Fig. 11. The upscale transformation is evident in the areal distribution (Fig. 11a), where the areas thresholded by rates > 7.6 mm h^{-1} maximize at subperiod 6. The convective rainfall area gradually decreases after subperiod 6, although the area thresholded

frequency of cloud-ground lightning discharges in ten Oklahoma MCCs was near this relative timing of maximum average precipitation rate.

Because of the similarity in trends of the A, R and V curves between the two gage-type samples, the averaged combined-gage analysis can be used to show the bulk precipitation characteristics without masking any important details. In Fig. 9, the combined-gage analysis is used to display these characteristics for all three domains, with the largest domain's values being an average of the indendent sample values in Fig. 8. The dominance of the smallest domain is evident through most of the MCC's life cycle. This small central region accounts for over half of the entire system's raining area over much of its lifetime, and it accounts for 59.2% of its cumulative rain volume (CV) over subperiods 3–12. The twice-as-large second domain contributes another 20.2% to CV. It is only during the decaying stages of the system, as the −54°C area shrinks toward sub-MCC dimensions, that the much larger third domain contributes appreciably to the raining area and to the remaining 20.6% of CV. From the average rate curves for the three domains, R is seen to be most intense when averaged over the smallest domain through most of the life cycle, due to generally smaller measurable values in the outer regions of the system.

A more detailed look of the rain intensity distribu-

PCP AREA, RATE, VOL   FULL MCC SAMPLE
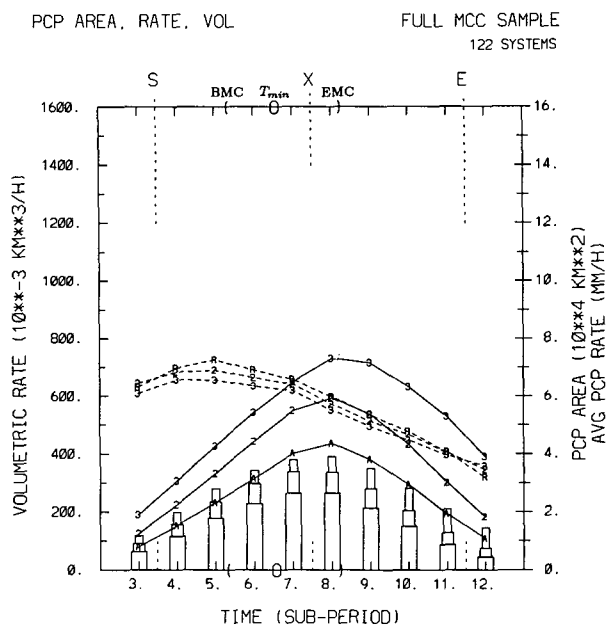   122 SYSTEMS

TIME (SUB-PERIOD)

FIG. 9. Bulk precipitation characteristics for 122-case composite MCC over all three domains, for combined-gage sample. Display is similar to Fig. 8. Primary curves are for smallest domain. Analysis for the midsize and largest domains are shown by the additional curves (labeled 2 and 3, and second and third departure bars, respectively).
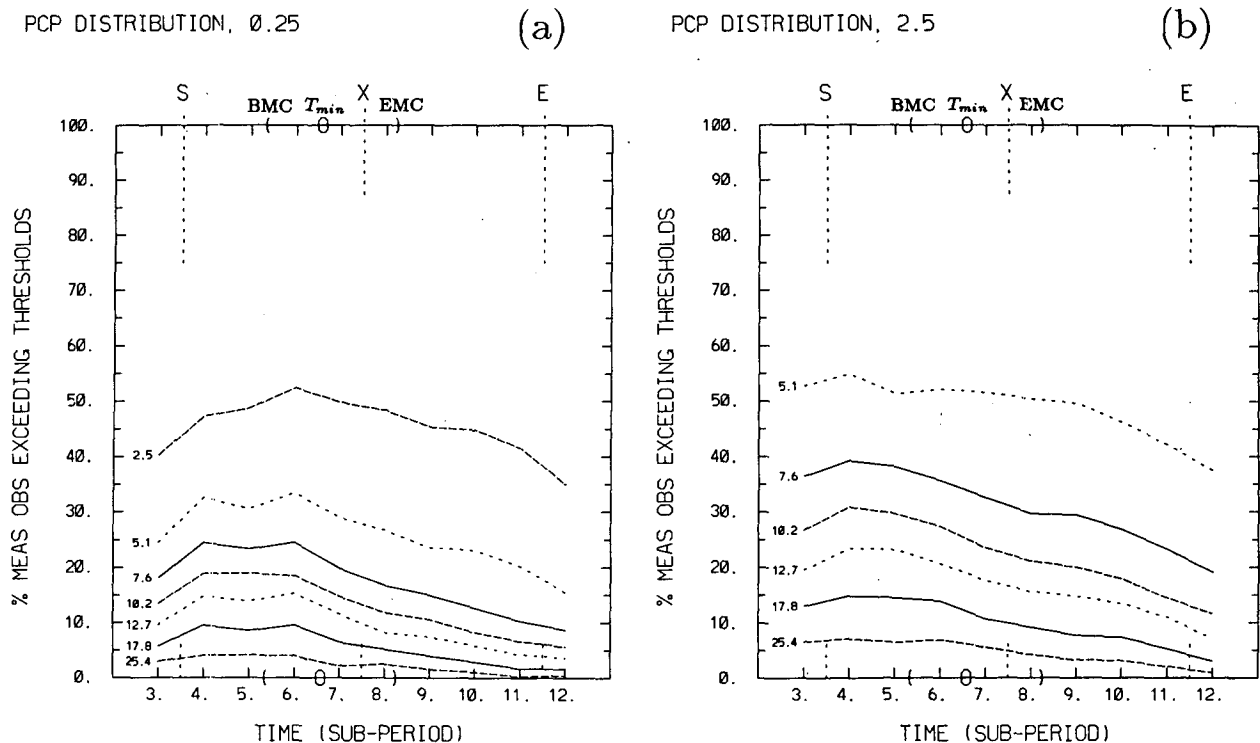
PCP DISTRIBUTION, 0.25 (a)   PCP DISTRIBUTION, 2.5 (b)

FIG. 10. Relative intensity distributions of measurable gage reports occurring in largest domain for 122-case composite MCC. Curves labeled in mm h^{-1} indicate percentage of reports at or exceeding that intensity. Analyses for (a) 0.25-mm gage sample, where 100% line represents 0.25-mm h^{-1} threshold, and (b) 2.5-mm gage sample, where 100% line is for 2.5-mm h^{-1} threshold. For each sample, the number of measurable reports increases from over 460 at subperiod 3 to about 1800 at subperiods 8 and 9, and decreases to 1100–1200 at subperiod 12.

by intensities < 7.6 mm h^{-1} continues to increase on through subperiod 8. This transformation from the relatively small maximum area of convective rainfall to the larger maximum of total rainfall area is concurrent with the progression of IR areal maxima as thresholded by colder-to-warmer IR temperatures through subperiods 6–8 in Fig. 4.

The volumetric-rate distribution in Fig. 11b similarly shows a peak by the more intense rainfall rates at subperiod 6, with the overall volumetric rate continuing to increase through subperiod 8. By making the rather crude assumption that all hourly reports ≥7.6 mm are due to convective rainfall and all those <7.6 mm are stratiform rain, the convective and stratiform components of the total volumetric rate can be quantified as indicated in Fig. 11b. While the convective precipitation peaks at subperiod 6, the stratiform portion steadily increases to subperiod 8 and very gradually tapers off thereafter; the two components are comparable toward the end of the life cycle. The stratiform contribution to the MCC's total cumulative volume is 36% (33% and 32% when CV is derived over the mid-size and smallest domains, respectively). Based on an alternate, higher convective/stratiform threshold of 10.2 mm h^{-1}, the stratiform component becomes

dominant by subperiod 9, and its contribution to the cumulative volume increases to 45%. (The stratiform contributions derived from the 0.25 and 2.5-mm gage-type samples alone are 2%–3% higher and lower, respectively.) This estimated range of the stratiform contribution is consistent with tropical studies of MCSs (Houze 1977; Gamache and Houze 1983; Houze and Rappaport 1984; Leary 1984), and with central United States MCSs described by Watson et al. (1988) and Rutledge and MacGorman (1988).

The IR-defined, intense *mesoconvective stage* discussed in section 2a, is seen in Fig. 4 to occur typically over the ~4-h spanning subperiods 6–8. The convective rainfall area and volumetric rate, as thresholded by any of the intensities 7.6–25.4 mm h^{-1} in Fig. 11, have larger magnitudes through these same three subperiods than earlier or later in the life-cycle. The term *mesoconvective* was chosen a posteriori to physically relate this large amount of convective precipitation to its IR signature, which is indicative of particularly strong, persistent, convectively forced divergence of cloudy air near the tropopause. Thus, on average, the *mesoconvective stage* appears to coincide with the MCC's upscale transformation evident in Fig. 11. The stratiform component steadily increases through this
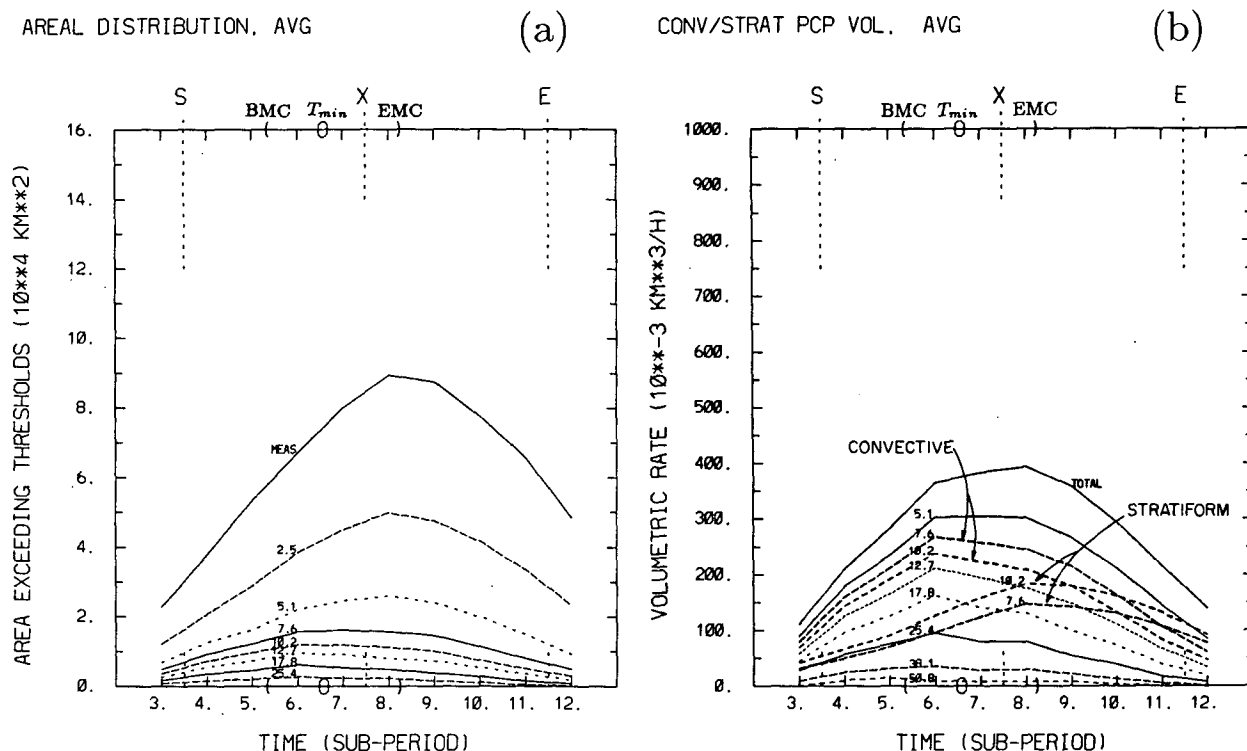
FIG. 11. Intensity distribution of measurable reports in terms of (a) area, and (b) volumetric rate, as thresholded by the labeled intensities (mm/h), for 122-case composite MCC. Values for each threshold are averages of the two independently derived values from the gage samples in Fig. 10, except for the total measurable area in (a), which is from the more sensitive 0.25-mm gage sample only. In (b), the volumetric rate curves due to intensities > 7.6 mm h^{-1} and >10.2 mm h^{-1} are estimates of convective precipitation, while the stratiform curves are the difference between the total and corresponding convective curves.

stage (Fig. 11b), and then persists for several more hours after the MCC decreases in convective intensity, loses its intense IR signature, and begins to decay. The IR-defined mesoscale *thermal minimum*, on average, occurs about midway through this stage, or 0.5–1.0 h after subperiod 6, when the convective volumetric rate is most intense (Fig. 11b).

b. Mapped precipitation analysis

The evolution of the composite rainfall pattern for the full MCC sample is shown in Fig. 12. The contoured field is the average of the two independent gage-type composite analyses of precipitation rate averaged over each grid cell (including reports of zero), or volumetric rate divided by the 69.5^2 km^2 grid-cell area. (Maximum contour values are much less than one might expect for a given case, both because of reports of zero within the same grid-cell being averaged in and because of case-to-case spatial variability of heavy precipitation.) At all subperiods in Fig. 12, the 0.5 mm h^{-1} contour is almost entirely well within the largest circular domain in Figs. 4–5, indicating that the domain indeed includes most of the significant MCC precipitation. This pattern reflects the evolution seen in the bulk precipitation

analysis: a relatively small, intense system early in the life cycle grows steadily as the area of lighter intensities expands, and then slowly diminishes in size and intensity.

Throughout the life cycle, the heaviest precipitation rate is displaced about 50–100 km to the right (generally south) of the track of the $-54°C$ cloud-shield centroid, and exceeds 5 mm h^{-1} through subperiods 4–8. Through subperiod 5, this displacement is southwest of the centroid, then southeastward during subperiods 6–8, and southwestward again thereafter. Since this analysis is a spatial smear of all the cases, about all it indicates is a preferred location for β-scale convective components to the south of the centroid. Otherwise, the patterns are fairly symmetrical, suggesting that no recurrent asymmetries exist in MCCs. This is perhaps in contrast to other MCS types. For instance, both midlatitude and tropical squall lines would likely exhibit a marked asymmetry, with greater rates shifted toward the leading edge of the overall precipitation pattern. This characteristic is seen in Fig. 12 only to a limited extent on the southeastern flank during the intense *mesoconvective* stage of subperiods 6–8, and probably reflects an unknown number of the sample cases which had a leading–squall line/trailing-strati-

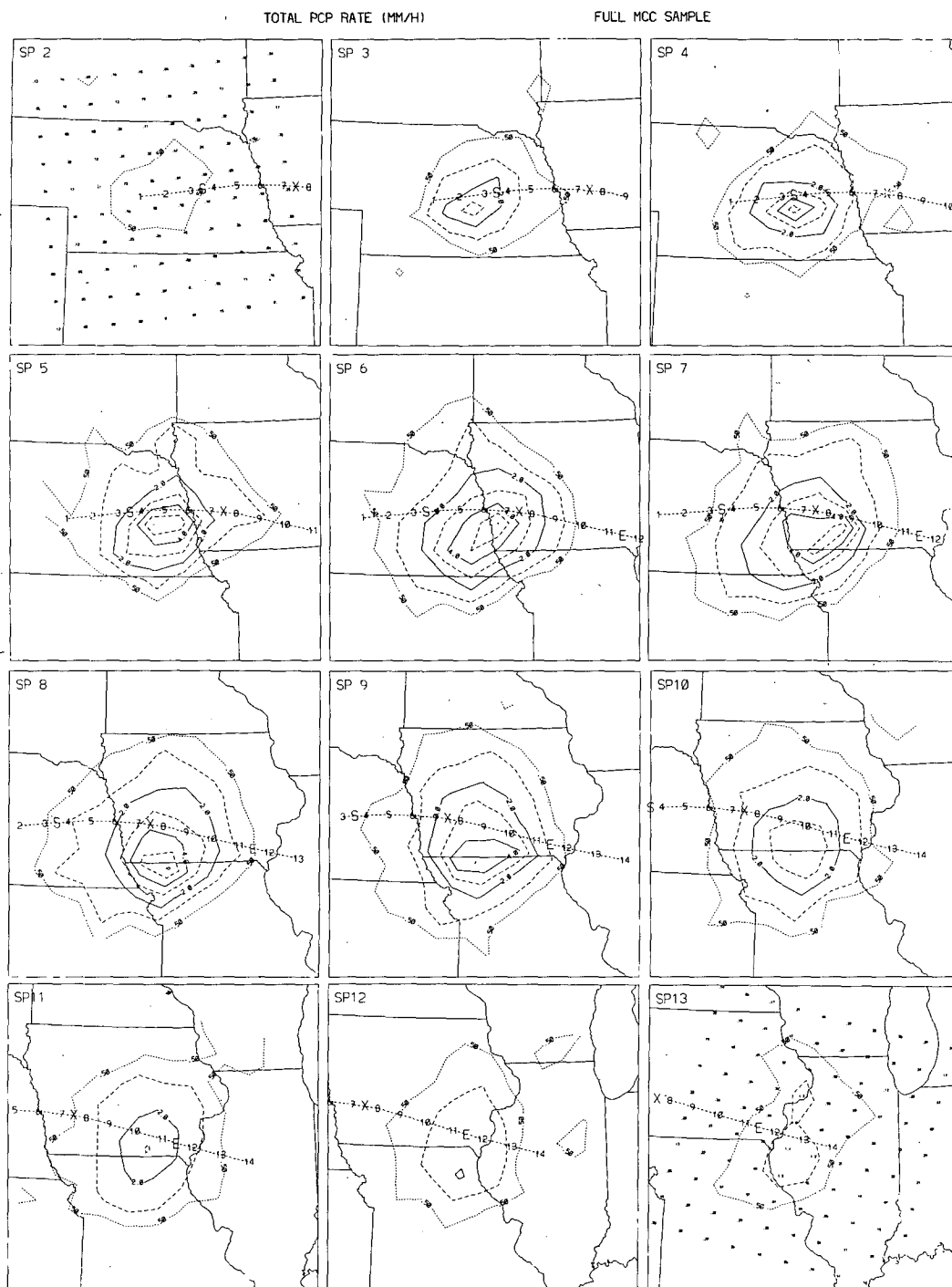TOTAL PCP RATE (MM/H)   FULL MCC SAMPLE

FIG. 12. Spatial patterns of precipitation rate over subperiods 2–13 for 122-case composite MCC, averaged over the two independent gage-type analyses. The average MCC track, with its subperiod positions marked, and relative map background are as in Fig. 5. As illustrated for subperiods 2 and 13, where the center of each 69.5×69.5 km^2 grid cell is indicated, the 10×10 analysis grid is centered on the MCC centroid at the respective subperiod, and the grid is rotated such that its x-axis is along the direction of MCC motion during that subperiod. Outer contour is 0.5 mm h^{-1}. Other contours are for integral values 1.0–6.0 mm h^{-1} (odd dashed, even solid).

form configuration, such as the MCC described by Smull and Houze (1985). A sample of 21 MCSs from May and June of 1985 included a third that were dominated by that type of structure (Blanchard and Watson 1986).

A partitioning of the composite precipitation pattern into convective and stratiform contributions, as thresholded by a rate of 10.2 mm h^{-1}, reflects this leading-line/trailing-stratiform structure more explicitly for subperiod 6 in Fig. 13a. The maximum composite convective rate is 4.9 mm h^{-1} (again, deceptively low due to the compositing technique), with the overall convective pattern shifted to the southeast of the centroid and the strongest gradient on the southeast flank. However, the southwestward trailing axis of the convective pattern also reflects a common convective substructure in MCCs in which the most vigorous convective regeneration is on the right-rear flank of the system (McAnelly and Cotton 1986). The stratiform precipitation pattern at subperiod 6, with a composite maximum of 1.7 mm h^{-1}, is more concentric and MCC-centered, and is shifted about 50 km to the west-northwest of the convective pattern. By subperiod 10 (Fig. 13b), the convective pattern has weakened and lost its leading-line semblance, and the stratiform pattern, still more MCC-centered and now shifted to the north-northwest of the convective pattern, has expanded and become dominant.

The evolution of the corresponding areal coverage pattern for the full sample composite (not shown) is very similar to that shown for precipitation rate in Fig. 12. At all subperiods, the outer fringe of the system (given approximately by the 0.5 mm h^{-1} contour in Fig. 12) is characterized by about a 10% coverage of measurable hourly reports (i.e., 90% of the gages had no precipitation). The maxima in the coverage patterns increase from 16% at subperiod 1 to ~65% for subperiods 5–11, and decrease to 21% at subperiod 14. (The independent gage-type mapped analyses show a similar bias in computing areal coverage as is evident in Fig. 8; the coverages cited here are averages of those independent analyses.) In general, these maxima are displaced 0–50 km to the south and west of the subperiod centroids, or about 50 km to the north or northwest of the maximum rates in Fig. 12.

The rainfall pattern for total life-cycle accumulation is shown in Fig. 14a. The axis of maximum precipitation reflects the persistent southward displacement of the maximum subperiod rates seen in Fig. 12, with the maximum composite accumulation of 23.7 mm occurring about 50 km south of the MCC's centroid at its IR-defined *maximum* extent. The pattern for areal coverage in Fig. 14b is very similar, and indicates a maximum coverage of 92% (i.e., only 8% of the gages in the composite grid cell to the southeast of the MCC *maximum* recorded no measurable precipitation). The spatial averaging of the 122 cases results in gridded composite areas in Fig. 14a that are smaller than in-
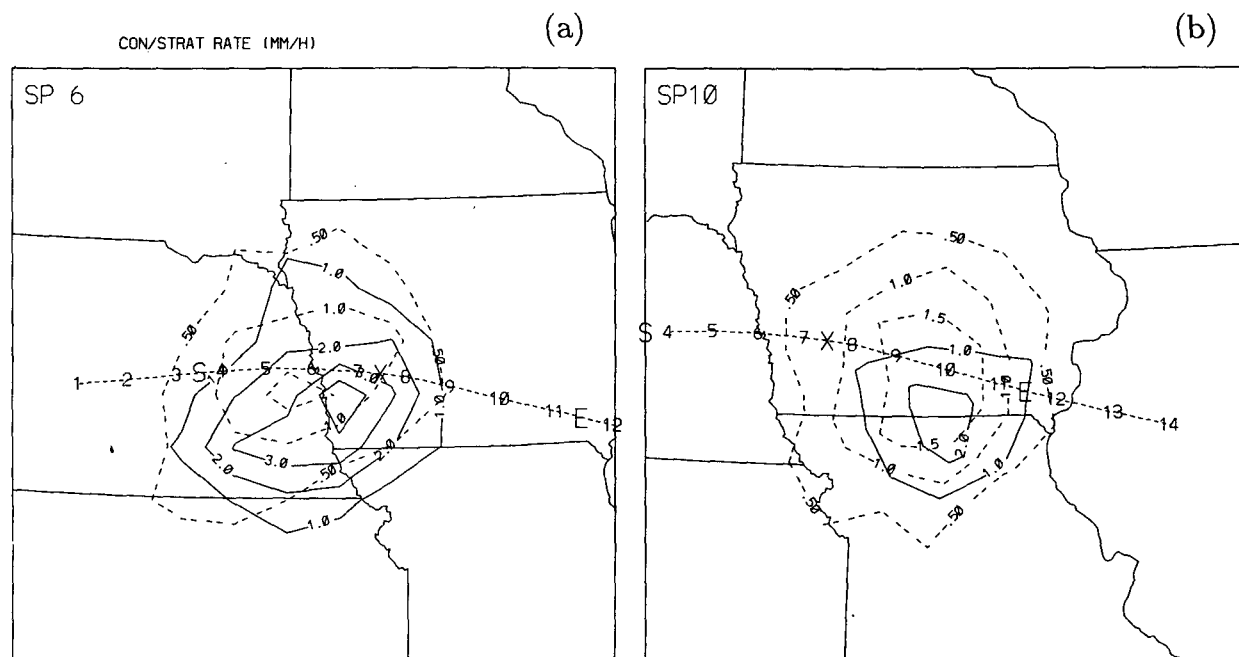
FIG. 13. Patterns of convective and stratiform precipitation rate for (a) subperiod 6 and (b) subperiod 10, based on threshold rate of 10.2 mm h^{-1}, for 122-case composite MCC. The grid-cell values are the composite volumetric rate due to convective/stratiform intensities, divided by the grid-cell area. Convective contours are solid and in intervals of 1 mm h^{-1}, and the stratiform contours are dashed and in 0.5 mm h^{-1} intervals.

TOTAL PCP (MM)   (a)   PCP COVERAGE (%)   (b)
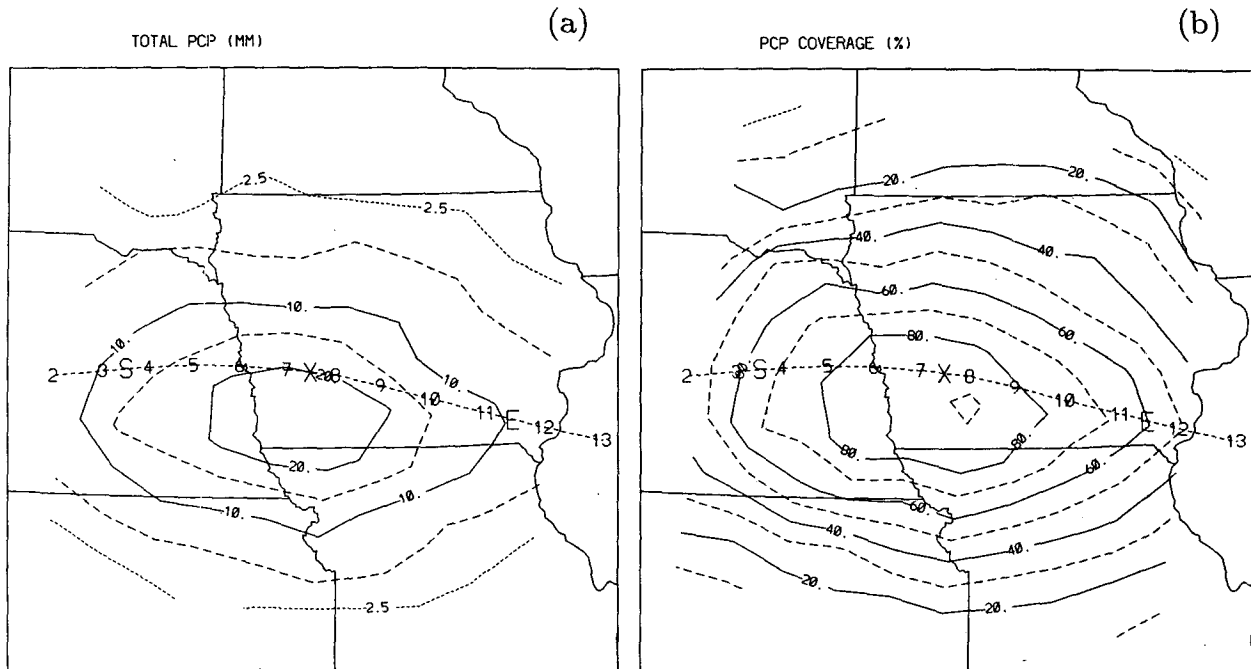

FIG. 14. Spatial patterns of (a) grid-cell-average, life-cycle precipitation (contours of 2.5, 5, 10, 15, and 20 mm) and (b) grid-cell coverage by measurable life-cycle precipitation (contours of 5% and 10%–90% at 10% intervals), derived from 122-case MCC sample, and relative to MCC *maximum* (X at center) and *start-to-end* (S–E) x-axis orientation. Analysis is shown for only the central 10 × 10 portion (as in Fig. 12) of a larger analysis grid.

dividual-case averages for accumulations > 10 mm, and larger than individual-case average area for lesser accumulations (curves 1 and C in Fig. 15). For instance, while the composite maximum in Fig. 14a is 23.7 mm for one grid cell of 4823 km^2, the average case produces grid-cell-average accumulations exceeding 25.4, 38.1, and 50.8 mm over gridded areas of 43 100, 18 600 and 8500 km^2, respectively. Conversely, while the gridded composite in Fig. 14a has measurable accumulation (>0.25 mm) over 1 018 000 km^2, the case-average area of measurable precipitation is only 320 000 km^2.

Despite the differences in data and analysis methodology used by KCF and herein, the total precipitation pattern in Fig. 14a is in general agreement with their "normalized composite precipitation pattern" (their Fig. 2). For instance, our composite x-axis, along the mean *start-end* velocity vector of 278° at 13.0 m s^{-1}, has a similar orientation as their x-axis (from 286°), which is aligned along their case-averaged "thermal wind vector in the cloud layer." The axis of maximum precipitation in both analyses is nearly parallel to and ~50–100 km south of the x-axis, with similar positions of the maxima.

The primary difference in the two analyses is an overall greater magnitude in KCF's composite pattern, as well as in their case-average statistics. Their composite maximum is 38 mm, compared with 23.7 mm in Fig. 14a. Similarly, their case-average areas exceeding
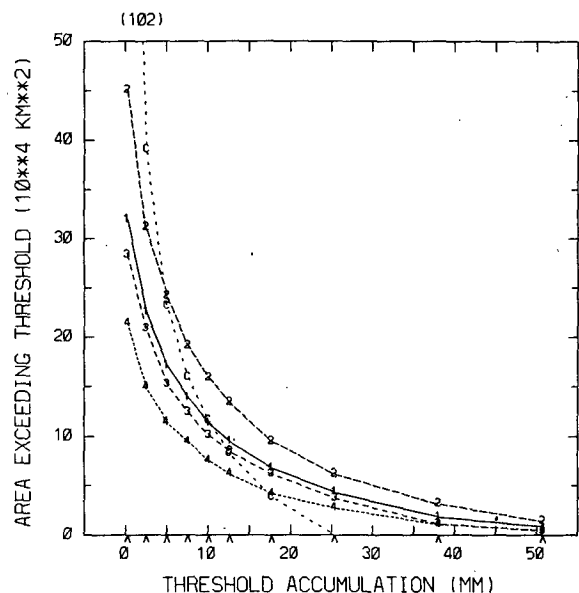
FIG. 15. Curves labeled 1–4: case-averaged gridded areas with total life-cycle precipitation accumulations exceeding various thresholds, with each curve representing a composite grouping of MCCs. Curve 1 is for full 122-case sample; curve 2 is for 41 large, high-rated cases; curve 3 is for 41 small, high-rated cases; and curve 4 is for 38 small, low-rated cases (curves 1–4 correspond to Table 2 entries A, E, D and B, respectively). Curve labeled C is derived from 122-case composite precipitation pattern from Fig. 14a. Pointers along x-axis show threshold values that were used. Area for curve C at lowest threshold is off the scale as indicated.

accumulations of 1, 26, and 51 mm exceed the corresponding case-average areas in our analysis (curve 1 in Fig. 15) by factors of 1.7, 2.6, and 3.7, respectively. Consequently, KCF derived an average precipitation depth of 16.1 mm, compared to our average of 10.8 mm, and their case-average total precipitation volume of 8.28 km^3 is more than twice as large as our average of 3.46 km^3. While it might seem that KCF's use of 24-h reports could have resulted in a systematic inflation of MCC precipitation estimates due to the inclusion of "non-MCC" rainfall along with MCC rainfall within the same 24-h period, it appears that they avoided this error by adjusting the 24-h reports with MCC accumulations derived from 1-h reports.

Instead, these differences can be largely attributed to several other factors. First, KCF's use of a denser network would result in a more thorough sampling of heavier precipitation, which would then be retained to a greater degree in their finer analysis mesh than in our grid. Secondly, as discussed earlier, our space–time domains are more conservatively defined than in KCF. Thirdly, our case selection process eliminated numerous prolonged or atypically evolving MCCs (such as with two intense *mesoconvective stages,* or involving a split or merger with another intense MCS) because they could not be fitted easily to the single growth/decay cycle typified in Fig. 4; such cases would produce more total rainfall than the average isolated, single-cycle case. Finally, KCF include springtime MCCs in their sample, which based on evidence therein and in Fritsch et al. (1986), are heavier-raining systems than those in June–August.

c. Discussion

The average precipitation life cycle of MCCs relates to a number of climatological studies of precipitation and convective phenomena over the central United States. Figure 2 illustrates the nocturnal predominance of MCCs, a fact well established in the annual summaries. Eighty-five percent of the systems reached their *maximum* from 2100–0700 CST,[7] with the average *start–maximum–end* period from ~2030–0145–0700 CST (Fig. 4). Because of this, and the large contribution by MCCs to total convective season (particularly summer) precipitation (Fritsch et al., 1986), then MCCs must account for much, if not most, of the convective season's well-known nocturnal maxima of precipitation amount and thunderstorm frequency (also thunderstorm duration) in this region (Kincer 1916; Means 1944; U.S. Weather Bureau and U.S. Corps of Engineers 1947).

Wallace's (1975) first-harmonic analysis of the diurnal variation of different classes of precipitation and thunderstorm frequencies over the United States provided the first clear picture of the nature of these nocturnal maxima. Subsequently, similar analyses utilizing longer records and/or denser observations have confirmed and described in more detail Wallace's findings (Easterling and Robinson 1985; Balling 1985; Riley et al. 1987; Winkler et al. 1988). Whereas the rest of the country generally has an early- to late-afternoon maximum frequency in June–August precipitation and thunderstorms, these studies show that the central United States has a marked, coherent (west to east) phase shift through the nocturnal period in the timing of these maxima. The western boundary of the nocturnal regime lies along the eastern slopes of the Rockies (approximated by the 1800 m terrain contour in Fig. 3), where the frequency maxima occur in late afternoon (~1800 LST). The maxima occur progressively into and through the nocturnal period eastward across the Plains states, with the less well-defined eastern boundary of this progression (several hundred kilometers east of the 300 m contour) characterized by maximum frequencies from ~2400–0600 LST for the various classes. The amplitudes of these first harmonics generally decrease from west to east across this region, such that (for instance) the early-evening maximum frequency of thunderstorms in the western plains is more pronounced than the midnight maximum frequency over Iowa. Furthermore, the harmonic amplitudes increase, and their maxima occur earlier in the nocturnal period, with increasing storm intensity, particularly in the eastern portions of the nocturnal regime.

These nocturnal precipitation and thunderstorm maximum frequencies are consistent with average MCC characteristics, including their diurnal timing, tracks, and precipitation life cycle. First, the general west-to-east track of MCCs across this region (Figs. 1, 5) through their nocturnal life cycle accounts for some of the phase shifting. (However, the phase speeds, i.e., the distance across the Plains divided by difference in phase, are faster than can be explained by the average MCC speed, especially for the more intense precipitation rates.) Second, the earlier occurring nocturnal maxima for more intense precipitation categories are related directly to the convective-to-stratiform transformation during the MCC's evolution (Figs. 10–11): Iowa's midnight thunderstorm maximum followed by its 0500 LST maximum frequency of precipitation (≥ trace) matches the average timing of this transformation. Third, the higher amplitudes of the first harmonics in the western plains are due to a stronger diurnal modulation of convection in that region. For instance, thunderstorms generally develop in the late afternoon east of the Rockies (or track off the foothills), then track eastward into the nocturnal period, either decaying or persisting as long-lived MCSs. Further east in the regime (e.g., Iowa), thunderstorms are more variably associated with locally generated, late-afternoon convection, and with MCCs and MCSs at various

---

[7] Central standard time is 6 h earlier than UTC, and can be considered local standard time (±1 h error) for MCC events.

nocturnal hours and stages of their life cycle, including some that track all the way from the High Plains through the nocturnal period (e.g., Wetzel et al. 1983; McAnelly and Cotton 1986).

Nocturnal MCCs also appear to be responsible for many severe flooding events in the eastern ⅔ of the country [Rodgers et al. (1985) and other annual summaries; Maddox et al. (1979)]. Crysler et al. (1982) showed that for four progressively severe categories of heavy rain, the maximum occurrence shifted from 1800 to 0200 LST. The 0100–0200 LST maximum frequency for their most severe category [>102 mm (8 h^{-1})] corresponds well to the average MCC's *mesoconvective stage* (from ~2300–0300 CST in Fig. 4).

Scofield (1987) developed a manual, operational method, based on MB-enhanced IR imagery, for making real-time estimates of heavy rainfall from such flood-producing MCCs and other types of convective storm systems. This technique assumes a generalized convective life-cycle model that is consistent with the average MCC life cycle seen here: heavier rainfall tends to occur during the cloud shield's growth stage and within the colder interior region, and much of the cloud shield is inactive and nonprecipitating. A "decision tree" provides empirical estimates based on this generalized model, and then a number of physical considerations are made which might amplify this first guess. Most of these amplification factors can occur in MCC-like systems, and some inherently differentiate them from smaller-scale systems. For instance, one of his original premises was that "clouds with cold tops that are becoming warmer produce little or no rainfall." However, Fig. 4 shows that this warming condition occurs after the mesoscale *thermal minimum* near subperiod 6–7, while the diminishing convective precipitation (Fig. 11) continues to contribute significant amounts until near the end of the life cycle. Thus, the "saturated environment factor", which relates to increased precipitation efficiency due to moistening by a long-lived storm, was included to account for systematic departures from this premise.

While Scofield's (1987) technique has emphasized real-time estimation of the heaviest precipitation in a convective system, he describes a relatively new operational procedure for making short-range (3-h) forecasts of a system's areal precipitation distribution. The procedure is based on the extrapolated or forecasted movement (e.g., Merritt and Fritsch 1984) of the current diagnosed precipitation pattern, modified by expected behavior of the convective system (e.g., Zipser 1982). It appears that the average MCC life cycle described herein could be incorporated into Scofield's "trend and expectancy guidelines" for forecasting MCC precipitation. A growing MCC that achieves an intense *mesoconvective* signature in the IR imagery could be forecasted (as a first guess) to follow an IR and precipitation evolution through the latter ~⅔ of an average MCC life cycle. As the system evolves, satellite,

raingage, and radar detection of subsequent life-cycle points (e.g., the succession of cold-to-warmer areal maxima in Fig. 4; the decrease in convective volumetric rate after subperiod 6 in Fig. 11b) would allow more confident prediction of the remaining life cycle.

A number of automated techniques, based on digital IR and/or visible imagery, also have been developed to estimate convective precipitation from the entire scale spectrum of storm systems. The simpler schemes assume that any life-cycle dependence on a cloud's precipitation rate is negligible compared to its dependence on instantaneous cloud top area and/or thermal structure [e.g., Doneaud et al. (1987); Negri et al. (1984); the "streamlined technique" of Griffith (1987)]. These schemes generally compute a cloud's volumetric rate V as a product of IR-thresholded area and a constant average rain rate, where the latter may be weighted by colder interior temperatures. These authors show that while V tends to have relatively large errors, the integration of a cloud's V through its lifetime (or large space–time integration of V over a population of clouds) is more accurate.

Both the "streamlined technique" of Griffith (1987) and the similar scheme of Negri et al. (1984) were testable for their ability to estimate V for the average MCC by using the IR life cycle in Fig. 4. (Several reasonable assumptions had to be made, including a maximum −20°C area consistent in time and magnitude with the colder maxima.) It was found that these simple schemes estimated values of V that were slightly higher than those observed in Figs. 8–9 for the first half of the life cycle, but tended toward overestimation by a factor of >2 at subperiod 12. The reason for the later-stage overestimation is the absence of a life-cycle dependence on average rate, which Figs. 8–9 show to decrease significantly through the last half of the life cycle. (These schemes' method of apportioning V over the coldest 50% of the cloud at variable intensities was found to spread it out over twice the observed precipitating area, with the maximum estimated rate less than half the average observed maximum. However, as seen in Fig. 8, comparing A and R is difficult because of their sensitivity to detection threshold. Thus, V is the more reliable variable for comparison.)

Griffith (1987) also has applied an automated, life-cycle-dependent method to rainfall estimation (including MCCs) over the central United States. Similar to Scofield's (1987) method, the volumetric rate (V) that it computes for a cloud is a function of cloud life cycle, such that greater V is inferred during growth. Based on the IR life cycle in Fig. 4, estimated V by her life-cycle method is ~4–5 times too large through subperiods 3–7 (peaking at subperiod 6 rather than 7 or 8), then decreases rapidly to less-than-observed after subperiod 10 and to near zero by subperiod 12.

An environmental modification factor (Griffith 1987) to these values could conceivably lower/raise the V estimates early/late in the life cycle toward the

observed V curve (based on an initial relatively dry environment that moistens through the life cycle), but the primary shortcoming of the method is in the assumed life-cycle parameterization. Griffith's three parameterized classes, based on a large sample of Florida clouds, are for clouds with maximum $-20°C$ areas <2000, 2000–10 000, and >10 000 km^2. The effects of these classes on V, from smallest to largest classes (Fig. 3 in Griffith, 1987), are toward a smaller estimated maximum (normalized to maximum cloud area), a later-occurring maximum, and larger estimates later into the life cycle. These trends, if extended to a parameterized cloud-size class more compatible with MCCs (maximum area > 100 000 km^2), would yield a V curve closer to that seen in Fig. 9. Such an extension would better reflect the prolonged *mesoconvective stage* in MCCs and the significant contribution of stratiform precipitation late into the life cycle.

4. Interstorm variability of precipitation characteristics

In the previous section, the average temporal and spatial evolution of the full 122-case sample was described. Of course, there is a large variability from one system to another, and it is important to understand how representative the composite analysis is of the typical case. In this section, we first examine the observed

variability of the overall sample. An error analysis of the sampling by the precipitation network and the analysis methodology then identifies the most accurate of the derived variables. Based on that information, we finally examine various subsets of the 122 cases that appear to exhibit significantly different characteristics from the full sample or from other subsets.

a. Variability of storm-total precipitation

Of the full 122-case sample, 101 MCCs had their complete life cycles occurring in the precipitation network, so that storm-total variables could be derived. Two scatter-plots showing the case distributions of such variables are given in Fig. 16, where the cases are distinguished between the relatively "ideal" and more "marginal" MCCs (high and low ratings), and between systems with maximum $-54°C$ areas larger and smaller than 200 000 km^2. As expected, the plots indicate that the larger systems tend to be "rainier", in terms of gridded measurable area and cumulative volume (Fig. 16a), and to a lesser extent in terms of the heavier rainfall variables of gridded area with accumulations exceeding 25.4 mm and maximum recorded precipitation (Fig. 16b). The correlation coefficient computed between maximum $-54°C$ area and each of the variables in Fig. 16a is about 0.65, but only about 0.45 for each of the variables in Fig. 16b.
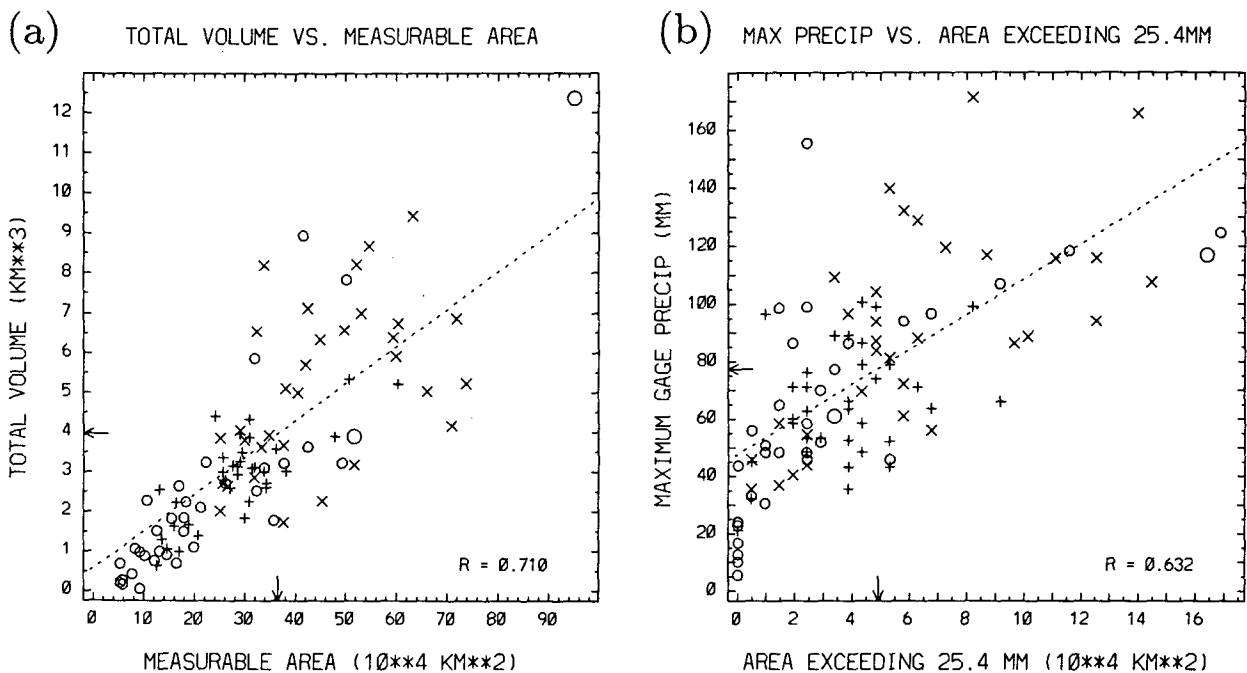

FIG. 16. Scatter diagrams of individual-case, total life-cycle precipitation variables, for the 101 MCCs that were completely within the precipitation network: (a) total precipitation volume vs gridded area of measurable precipitation, and (b) single-gage maximum precipitation accumulation vs gridded area with precipitation > 25.4 mm. In both diagrams, 'X' denotes large (maximum IR areas ≥ 200 000 km^2), higher-rated MCCs from Fig. 2, '+' denotes small (<200 000 km^2), higher-rated MCCs from Fig. 2, and the large and small circles denote the lower-rated, large and small systems, respectively, from Fig. 2. For the 66 higher-rated systems, the case average of each variable is indicated by an arrow, the least-squares line of regression is indicated by the dotted line, and the correlation coefficient (R) is given.

The scatter-plots indicate that the low-rated, smaller systems (small circles) tend to be the "least rainy", in terms of both total area and volume, and heavier rainfall; these systems result in a marked positive skewness in the full-sample distribution over each of the variables. The low-rated systems (large and small) also account for a few outlying cases on the large end of the scales in Fig. 16 (and in Fig. 2). Thus, the high-rated sample of 82 systems (66 with complete life-cycle documentation) is more representative of the "rainier" and more idealized MCC than the full sample, and its distributions over the variables are less skewed. The averages and correlations between each pair of variables shown in Fig. 16 are based on this higher-rated sample, as is the statistical discussion of case variability below.

Even by eliminating the lower-rated and generally less rainy systems from our sample, the average of each of the four storm-total variables in Fig. 16 is much smaller than that derived by KCF. For instance, our average point maximum rainfall is 77.4 mm (Fig. 16b), compared to KCF's average of 104 mm. However, the median (89 mm) and mode (75 mm) that they cite for their cases are much closer to our average. Indeed, scatter-plots presented by Fritsch et al. (1986; their Figs. 7–8) of storm maximum precipitation vs. area of >25 mm, for the same 74 cases studied by KCF, show that several extremely "rainy" systems lie well removed from the bulk of their cases, with their main clustering being very similar to our distribution in Fig. 16b. Based on this comparison, and on monthly statistics presented by both KCF and Fritsch et al. (1986), we infer that most of the outlying, rainiest systems they studied are pre-June MCCs that we excluded from our sample. Thus, our analysis is more consistent with their summertime sample than would be inferred by comparing overall averages alone, and remaining differences can likely be explained by the differing analysis methodologies, as discussed earlier.

b. Variability and error analysis of subperiod precipitation

The large interstorm variability evident in total life-cycle variables in Fig. 16 is also evident in the time-dependent subperiod precipitation variables. This variability is illustrated in Fig. 17a–c for the high-rated sample, where the combined-gage, large-domain curves of case-averaged A, R and V versus subperiod are shown, along with their standard deviations ($\pm\sigma$, full dotted bars). Averaged over the eight mature subperiods (4–11), σ_A, σ_R and σ_V are 46.3%, 28.3%, and 54.8%, respectively, of their subperiod average values. The large σ_A is expected for most of the composite life cycle because of the large range in storm sizes. The smaller σ_R implies that the average precipitation rate tends to be relatively more stable from case to case. Since $V = AR$, its variance is larger due to the combined variances of A and R: $\sigma_V^2 \approx \sigma_A^2 + \sigma_R^2$.

Due to case-to-case variability in the relative timing of maximum A, R and V, the maxima in the composite subperiod curves are less than the average maximum values derived for the individual cases. This is illustrated in Fig. 17 by the case average of maximum hourly A, R and V (using the 1–2–1 smoothed hourly values), denoted by C at their average relative timing coordinate. For A and V, the average maximum hourly value is 8.4% and 18.2% larger, respectively, than the maxima of the subperiod curves, while the hourly maximum for R is 31.7% larger than its subperiod maximum. This suggests that, temporally, the A and V curves are both more representative of the average MCC than is the R curve. This is confirmed by the variability in the timing of these hourly maxima, as indicated by the horizontal $\pm\sigma$ timing bars (dashed) in Fig. 17: for A and V, $\sigma \approx 1.5$–1.8 subperiods, while for R, $\sigma \approx 2.5$ subperiods. Thus, maximum R is more variable in a temporal sense, with the composite trends in R smoothing out much of this case-to-case variability.

A fraction of the observed case-to-case variability seen in Fig. 17 is real, while the remaining part is due to inadequate sampling by the sparse network. To evaluate these relative contributions, a model MCC was prescribed by the characteristics of the 82-case, high-rated composite MCC, including its time-dependent velocity, cloud-shield area, and precipitation intensity distributions as compiled from each gage-type sample over each of the three annular bulk analysis regions. For each annular region, these distributions were arbitrarily specified as concentric rings, with intensity decreasing with radius, and with each ring representing a discrete hourly value at 0.25- or 2.5-mm increments and having an area proportional to its observed relative frequency. This model MCC was initialized at 176 locations in the network, providing a large number of random samplings of the same storm. Each run was analyzed identically as described in section 2b, with each observation site in Fig. 3 assigned an hourly value based on its gage type and its relative position in the prescribed storm. These 176 realizations were then averaged to produce a simulated composite MCC, whose case-averaged subperiod values of A, R and V were, indeed, almost identical to the real 82-case composite.

The "case-to-case" variability of this simulated MCC, due totally to network sampling variability, is shown in Fig. 17 by the solid error bars ($\pm\sigma_{Network}$). Averaged over the eight mature subperiods, $\sigma_{Network}$ (relative to the subperiod average) is 13.6%, 18.1%, and 23.5%, for A, R and V, respectively, each considerably less than the total observed deviation (σ_{Total}). Similar experiments, with model storms based on various composite groupings of MCCs, showed that the relative $\sigma_{Network}$ of all of the variables decreased with increasing model storm size, due to increased sampling by the network. A sparser sampling in the western
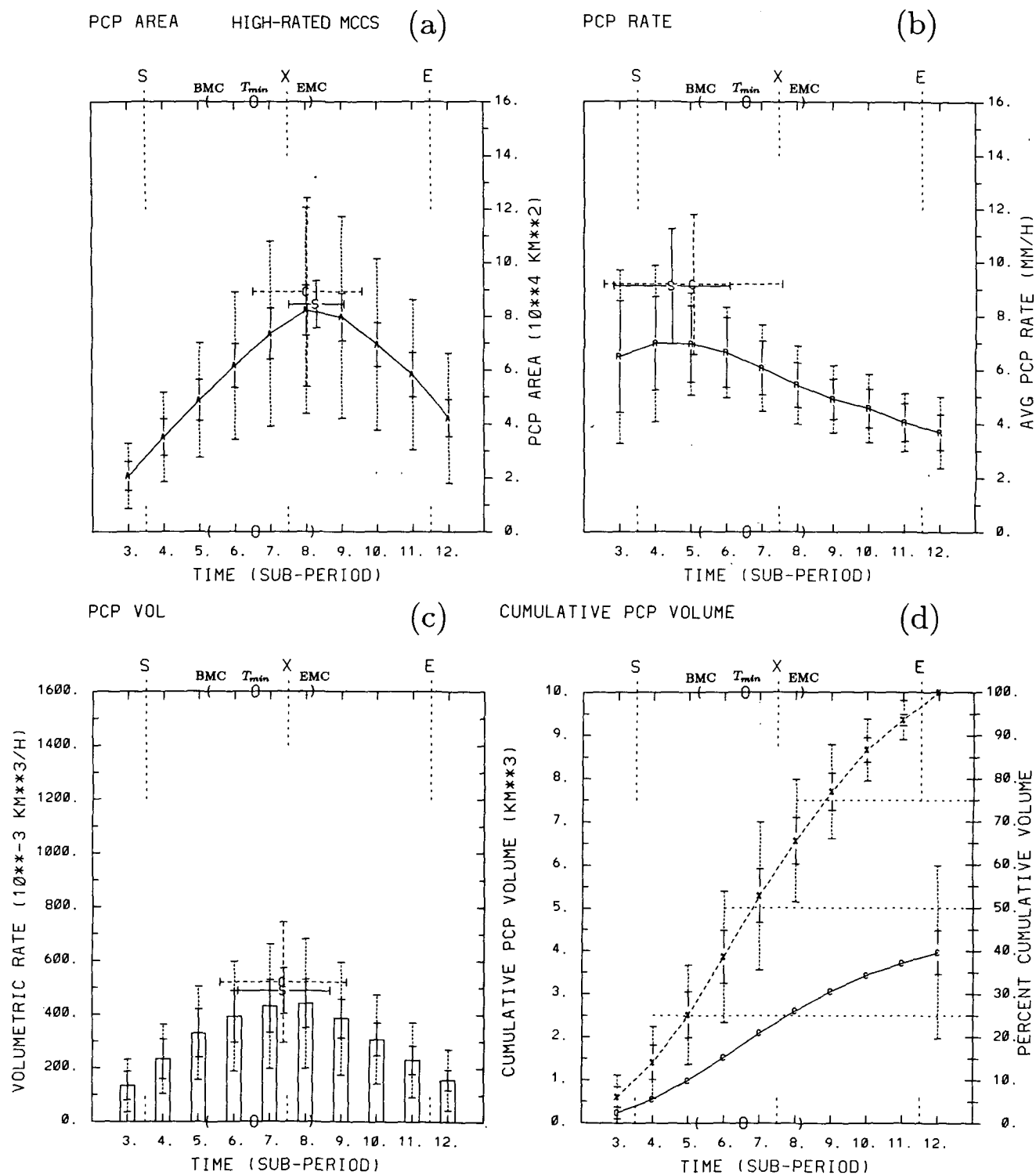
PCP AREA   HIGH-RATED MCCS   (a)   PCP RATE   (b)

PCP VOL   (c)   CUMULATIVE PCP VOLUME   (d)

FIG. 17. Combined-gage, large-domain analyses of A, R, V and CV (a–d, respectively), for 82-case, high-rated composite MCC. Standard deviations ($\pm\sigma$) for subperiod values are shown by dotted vertical error bars (subperiod deviations for CV are indicated on the dashed curve for percent cumulative volume, except for subperiod 12, where it is indicated for the solid absolute curve). The case-averaged magnitude and timing of maximum hourly A, R and V is indicated in the respective panels by C, along with their $\pm\sigma$ bars (dashed) for magnitude and timing. The solid portions of the subperiod $\pm\sigma$ bars indicate the deviations due to sampling error, derived from a simulated MCC experiment (see text). The simulated, case-averaged maximum hourly value and timing of A, R and V is indicated by S, along with their $\pm\sigma$ bars (solid) for magnitude and timing.

plains (Fig. 3) was similarly found to increase σ_{Network} for more western-occurring systems [as well as introducing slight biases ($\leqslant 7\%$) relative to the better-sampled systems further east]. However, the least accurately measured model storm, based on the small, low-rated MCCs, had average relative σ_{Network} values that were <10% larger than those above, indicating that even the "drier", small MCCs are measured fairly accurately by the network.

For the high-rated composite in Fig. 17, the amount of total observed variance accounted for by network sampling error [$\sigma^2_{\text{Network}}/\sigma^2_{\text{Total}}$ ($\times 100\%$)], averaged over the eight mature subperiods, is 9.0%, 41.6%, and 19.1% for A, R and V, respectively. Thus, A is measured most accurately by the network, and R least accurately. The variability of the simulated maximum hourly values (denoted by S and solid error bars) likewise indicates that the network can measure the magnitude and time of maximum A relatively accurately. For maximum V, the magnitude is measured more accurately than its timing; neither the magnitude nor timing for maximum R is measured very well. Figure 17d shows that the total cumulative volume (at subperiod 12) is measured particularly accurately; only 6.3% of its total observed variance is due to sampling error. This accuracy is probably due to the cancellation of opposite-sign errors in V during its life-cycle integration.

In summary, there is a large case-to-case variability in the observed bulk precipitation characteristics. This variability is most reliably detected for CV. Precipitating area A is the most reliably measured of the subperiod variables, and this accuracy carries through to the gridded area of life-cycle accumulation, particularly as thresholded by smaller values. Average rate R is the most poorly measured, due to inadequate sampling of intense convective rainfall. Thus, it should be easiest to demonstrate differences between various classes of MCCs by concentrating on A and CV. It should be noted that for both the real and simulated composite MCC, all σ values (relative to their means) were less for the combined-gage sample than for either of the independent gage-type samples. The simulation experiment also showed that the combined-gage sample reduced the sampling error variance. Thus, while the combined-gage analysis smooths the gage biases evident in Fig. 8, we emphasize it because of its ability to better estimate case variability.

c. Comparison of composite subsets of MCCs

About 100 subsets of the 122 MCC cases were identified based on a number of criteria, e.g., maximum cloud-shield size, rating, duration, storm speed and direction, diurnal timing, geographical location, and month. All subset composites displayed the same trends in A, R and V as did the full-set composite illustrated in Figs. 8 and 9, with their maxima occurring generally as subperiod 8 (± 1 subperiod) for A, at subperiod 8

or 7 for V, and, more variably, at subperiods 3–6 for R. The composite patterns of subperiod and total life-cycle precipitation for these subsets were also, in general, quite similar to the full sample's composite patterns in Figs. 12–14. This general similarity between composite groupings is consistent with KCF's study, which found no significant differences in composite total precipitation pattern, nor in its inferred temporal distribution, between four groupings of MCCs based on synoptic classifications.

Despite the general similarity in the precipitation life cycles displayed by these subset groupings, a few subsets showed significant differences in the magnitudes of the precipitation variables. These composite subsets are summarized in Table 2, where entry A is the full 122-case composite. As discussed earlier, the small, low-rated systems tended to be drier (Fig. 16), so that its composite (entry B, including all low-rated cases in Fig. 2 except the two very large ones), had low magnitudes for all the parameters listed in Table 2. For instance, it produced 2211 units (10^{-3} km^3) of total precipitation volume CV, compared to 2865 units produced by the sample of high-rated but similar-sized MCCs (entry D). A comparison of the areal distribution of CV between these two small-system composites (curves 3 and 4 in Fig. 15) shows that while the low-rated systems, on average, produced accumulations $\geqslant 38.1$ mm over as much area as the small, high-rated composite, their lesser degree of organization resulted in a smaller areal extent of smaller accumulations. By excluding the low-rated systems, all of the parameters in Table 2 become greater for the high-rated composite (entry C) than the full-sample composite (entry A). All of the composite subsets in Table 2 after entry B include only high-rated systems.

Very large differences exist between the subsets of MCCs with maximum $-54°C$ areas less than and greater than 200 000 km^2 (entries D and E in Table 2), as shown also in Fig. 16. Based on a two-way Student t distribution (Panofsky and Brier 1968), the large and small composites have significantly different average values of maximum hourly A and V, and of total cumulative volume CV, at the 99.9% confidence levels. This is not unexpected, of course, since larger storms, on average, would be precipitating more water mass over a larger area than smaller storms, and by lasting over 2-h longer than the small systems (Table 2), would produce much more total rainfall.

Less expected is that the large composite's average rate R is larger than the small composite's R through the first two-thirds of the life cycle, and that its mean maximum hourly R in Table 2 is significantly larger at the 95% confidence level. This suggests that for an MCS to develop into a large MCC, its early meso-β-scale convective clusters need to be more intense than in small systems. Moreover, it suggests that once they are fully developed, a greater proportion of intense convective rainfall persists in the large MCCs. This

TABLE 2. Characteristics of various composite groupings of MCCs. Bulk rainfall entries
are based on combined-gage, large-domain analysis.

| | Composite grouping | | Satellite characteristics[a] | | | Bulk precipitation characteristics[b] | | | |
| | | | Maximum IR area (10^3 km^3) | | Mature duration (h) | Max hourly precip values[c] | | | Total precip volume (10^{-3} km^3) |
	Description	Cases (complete cases)	−54°C	−33°C		Area (10^4 km^2)	Avg./rate (mm/h)	Vol rate (10^{-3} km^3/h)	
A	Full set	122 (101)	186	302	10.49	8.03	9.06	463	3462
B	Low-raters (small)	38 (34)	129	220	9.24	5.77	8.82	326	2211
C	High-raters	82 (66)	206	331	10.94	8.91	9.19	519	3971
D	Small	41 (34)	149	253	9.79	7.04	8.53	415	2865
E	Large	41 (32)	263	407	12.08	10.90	9.89	631	5146
F	Western-large[d]	11 (9)	262	389	13.68	9.90	8.98	527	4395
G	Central-large	14 (10)	269	417	12.69	9.49	9.97	596	4982
H	Eastern-large	16 (13)	260	411	10.45	13.05	10.03	749	5946

[a] Based on total number of cases.
[b] Based on number of complete life-cycle cases.
[c] Based on 1–2–1 temporally smoothed hourly values.
[d] Bulk precipitation figures are adjusted for network biases.

could be due to 1) a larger and more intense mesoscale circulation that better supports deep convection in the large systems, 2) a larger core region in which subcloud evaporation is significantly reduced, and/or 3) simply stronger environmental forcing (e.g., a more unstable air-mass, stronger large-scale lifting, or greater moisture influx by low-level jet). The larger proportion of intense convection in the large MCCs is also evident in the thresholded areas of total rainfall in Fig. 15 (curves 2–3): for areas with ⩽25.4 mm, the ratio of large to small MCC area is relatively constant at ~1.5–1.6, but increases to 3.3 for accumulations ⩾ 50.8 mm.

A stratification of the MCCs based on their *starting* longitude, showed no significant longitudinal dependence of the bulk precipitation characteristics for the small MCCs, but a definite tendency for the large systems to be rainier with a more eastern longitude. This is shown by entries F, G and H in Table 2, which are western, central and eastern subsets of the large, high-rated set (*starting* west of 100°W, between 100° and 95°W, and east of 95°W, respectively)[8]. There is a general west-to-east increase in the magnitude of all the precipitation characteristics in Table 2, with the eastern composite's average maximum A and V significantly larger than for the western composite (at the 95% level). In spite of the eastern composite being 3.2-h shorter in duration than the western composite, it produces significantly more total volume (90% level).

However, the linear correlation between *starting* longitude and CV is only ~0.3 for this sample of large systems.

This tendency for the large eastern systems to be rainier than western systems supports the findings of McAnelly and Cotton (1986) that were based on a smaller sample. Furthermore, they found that the growth of the large, western MCCs on the High Plains involved a more chaotic substructure and evolution than the large, eastern MCCs developing over the Mississippi River basin. This is also supported by the composite precipitation patterns derived from the larger sample in the current study. In Fig. 18, the patterns of the large systems *starting* west of and east of 97.5°W show that the eastern MCCs, indeed, have a larger, and more coherent and consolidated core of heavier precipitation. The western half of small systems, while not being significantly different from the eastern half in terms of magnitude of the bulk precipitation characteristics, also showed a less coherent and more elongated pattern of composite total precipitation than the small eastern composite (not shown). It is also seen from Fig. 18 (and also for the small west/east stratification) that the eastern systems, on average, moved on a more southeastward track than the western MCCs. In fact, a stratification based explicitly on northeastward *vs.* southeastward moving MCCs shows composite patterns very similar to those in Fig. 18a and 18b, respectively.

Similar investigation of composite MCCs based on their latitude showed no latitudinal dependence of their precipitation characteristics. This is in contrast to Fritsch et al. (1986), who found that total MCS precipitation decreases with latitude, presumably due in part to their increased distance from the Gulf of Mexico. However, much of their latitudinal dependence can, in fact, be attributed to a seasonal depen-
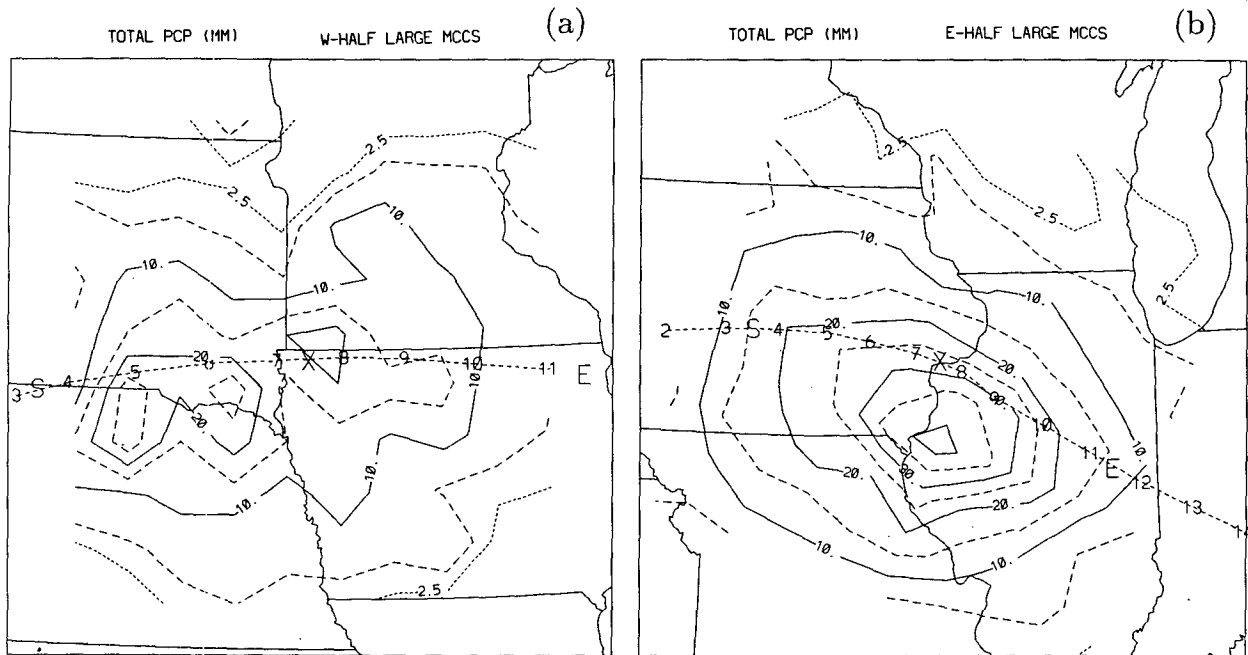
---

[8] This tendency far exceeds the biases introduced by sparser sampling of the western systems. The discussion here considers the adjusted figures for the western-large composite in Table 2 (entry F). The corrections were derived from comparisons of three simulated composite MCCs (western, central, and eastern), each based on 55 samplings of a model MCC having the characteristics of entry E in Table 2. (Section 4b describes the simulation technique.) A, V and CV were adjusted upward by ~5%–6%, and R downward by ~7%.

FIG. 18. Composite, total life-cycle precipitation pattern for (a) western half of large MCC sample, and (b) eastern half of large MCCs, based on a *starting* longitude west and east of 97.5°W, respectively. Details are as in Fig. 14a.

dence: springtime systems, which they and KCF showed to be rainier, tend to occur at more southern latitudes. By excluding pre-June MCCs, and by screening out many southern cases that failed to display a typical evolution (note from Fig. 1 the sparsity of systems in the Gulf Coast states), our sample consists of a set of less baroclinic MCCs, characterized by a well-organized, single growth/decay cycle, which shows no such latitudinal dependence.

A number of other stratifications (diurnal timing, month, etc.) showed no significant differences in their bulk precipitation characteristics. We did not attempt to stratify the systems according to any synoptic criteria, as did KCF in their analysis of four synoptic classes of MCCs. However, only their composite of "synoptic" events was significantly rainier than their overall composite, and 55% of those cases occurred before June. Their next rainiest category, "frontal" events, consisted of 34% pre-June cases. Thus, their remaining cases and composites are more consistent with our June–August sample.

5. Conclusions

From a 7-year compilation of MCC climatology (e.g., Rodgers et al., 1985), we screened 122 cases occurring in June–August that displayed a typical evolution as viewed by satellite. This evolution is characterized by a single and well-organized meso-α-scale growth/decay cycle, and a relative isolation from any other significant precipitating cloud shields. The screening specifically eliminated all pre-June cases,

which generally occur in a more baroclinic environment, and also at more southern latitudes. It also eliminated many other cases that, for various reasons, evolved too atypically to be considered representative events. Our sample consists primarily, then, of the types of systems that, as KCF noted, become most common in mid to late summer, and whose "rain area may be more dependent upon the latent heat release and internal dynamics of the convective systems than in the spring."

Hourly precipitation data associated with each MCC were analyzed in a time and space-dependent context relative to its normalized, satellite-defined life cycle (Figs. 4, 5), and the individual-case analyses were averaged to reveal the composite precipitation evolution for the entire sample (Figs. 8, 9). The average hourly precipitation area (A) increases throughout the growth phase of the MCC and reaches a maximum about 1-h after the *maximum* cloud-shield area (based on $-54°C$ IR threshold). The average precipitation intensity (R) in this hourly area is relatively high through most of the MCC's growth stage, reaching a maximum, on average, 1–2 h after its *start*, when the proportion of intense convective precipitation rates is also large (Fig. 10). The volumetric precipitation rate (V) is more symmetrically distributed in time and reaches a maximum, on average, at about the time of the *maximum* cloud-shield area.

The time period from maximum R, through maximum V, and to maximum A, corresponds to the average timing of an IR-defined, intense *mesoconvective*

stage. Essentially, it is this characteristic IR signature, typically lasting ~4 h, that uniquely identifies the MCC as an intense (cold-topped), well-organized α-scale system. The area and volume of convective intensities (>7.6 mm/h) reach their maxima early in this stage and then remain high through it; during this stage, a large area of stratiform intensities is also generated. The stratiform component persists and becomes increasingly dominant as the convective precipitation subsides through the latter stages of the life cycle.

The time-dependent, composite precipitation pattern (Figs. 12, 13) reflects this evolution in spatial form: a small, intense system grows steadily into a larger, less intense system, and then slowly shrinks. Throughout the life cycle, the maximum in the precipitation pattern is displaced 50–100 km south of the −54°C cloud-shield centroid, so that the axis of maximum life-cycle accumulation (Fig. 14a) is approximately parallel to and south of the centroid track. This storm-total pattern is consistent with that found by KCF.

Of the average total precipitation volume produced by the MCCs, 36% was due to intensities < 7.6 mm h^{-1}, and 45% due to intensities < 10.2 mm h^{-1} (time integral of curves in Fig. 11b). This can be considered an estimated range for the stratiform contribution to MCC precipitation, and agrees well with studies of tropical MCSs (Houze 1977; Gamache and Houze 1983; Houze and Rappaport 1984; Leary 1984). The evolution of the convective vs. stratiform precipitation pattern (Fig. 13) shows that the axis of convective precipitation tends to arc from the eastern through southern and southwestern flanks of the system, 50–100 km from the centroid. The stratiform pattern is more concentric and MCC-centered, and tends to be displaced ~50 km to the west through north of the convective pattern. During the intense *mesoconvective stage,* these composite patterns resemble a leading-squall-line/trailing-stratiform configuration, with the most intense convection on the southeastern flank of the system.

A stratification of the MCCs into various subsets revealed several significantly different classes: 1) the small, less-organized systems were "drier" than the similar sized but better-organized MCCs; 2) large systems are "rainier" than smaller ones, as expected; 3) large, eastern systems were "rainier" than large western MCCs, but not so for small MCCs; and 4) the eastern systems, both large and small, had a more coherent and intense core of heavy precipitation through its life cycle than the western systems, presumably due to a more steady-state, less chaotic evolution of the convective substructure.

This life cycle reveals explicitly the temporal nature of MCC precipitation that was only inferred by KCF in their composite analysis of total MCC rainfall patterns. The only general difference between the storm-total precipitation characteristics derived from this study and by KCF is that theirs indicates more precipitation over a larger area, resulting in a case average of over twice as much total volume. This difference is primarily due to 1) our elimination of springtime (pre-June) cases and other "rainier-than-average" MCCs that evolved anomalously, and 2) the more conservative space–time domain that we used to define MCC precipitation.

REFERENCES

Augustine, J. A., 1985: An automated method for the documentation of cloud-top characteristics of mesoscale convective systems. NOAA Tech. Memo. ERL ESG-10, U.S. Dept. Commerce, National Oceanic and Atmospheric Administration, Environmental Research Laboratories, Environmental Sciences Group, Weather Research Program, Boulder, CO 80303, 121 pp.

——, and K. W. Howard, 1988: Mesoscale convective complexes over the United States during 1985. *Mon. Wea. Rev.,* **116,** 685–701.

Balling, R. C., Jr., 1985: Warm season nocturnal precipitation in the Great Plains of the United States. *J. Climate Appl. Meteor.,* **24,** 1383–1387.

Blanchard, D. O., and A. I. Watson, 1986: Modes of mesoscale convection observed during the Pre-STORM Program. Preprints, *Joint Sessions 23rd Conf. on Radar Meteor. and Conf. on Cloud Phys.,* **3,** Amer. Meteor. Soc., Snowmass, J155–J158.

Clark, J. D., Ed., 1983: *The GOES User's Guide.* U.S. Dept. Commerce, National Oceanic and Atmospheric Administration, National Environmental Satellite, Data, and Information Service, Office of Satellite Data Processing and Distribution, 167 pp. [NTIS No. PB84-104413]

——, A. J. Lindner, R. Borneman and R. E. Bell, 1980: Satellite observed cloud patterns associated with excessive precipitation outbreaks. Preprints, *Eighth Conf. on Wea. Forecasting and Analysis,* Amer. Meteor. Soc., Denver, 463–473.

Crysler, K. A., R. A. Maddox, L. R. Hoxit and B. M. Muller, 1982: Diurnal distribution of very heavy precipitation over the central and eastern United States. *Natl. Wea. Dig.,* **7,** 33–37.

Doneaud, A. A., J. R. Miller, Jr., L. R. Johnson, T. H. Vonder Haar and P. Laybe, 1987: The area-time-integral technique to estimate convective rain volumes over areas applied to satellite data—a preliminary investigation. *J. Climate Appl. Meteor.,* **26,** 156–169.

Easterling, D. R., and P. J. Robinson, 1985: The diurnal variation of thunderstorm activity in the United States. *J. Climate Appl. Meteor.,* **24,** 1048–1058.

Fortune, M. A., and R. L. McAnelly, 1986: The evolution of two mesoscale convective complexes with different patterns of convective organization. Preprints, *Joint Sessions 23rd Conf. on Radar Meteor. and Conf. on Cloud Phys.,* **3,** Amer. Meteor. Soc., Snowmass, J175–J178.

Fritsch, J. M., and R. A. Maddox, 1981: Convectively driven me-

soscale weather systems aloft. Part I: Observations. Part II: Numerical simulations. *J. Appl. Meteor.,* **20,** 9–26.

——, R. J. Kane and C. R. Chelius, 1986: The contribution of mesoscale convective weather systems to the warm-season precipitation in the United States. *J. Climate Appl. Meteor.,* **25,** 1333–1345.

Gamache, J. F., and R. A. Houze, Jr., 1983: Water budget of a mesoscale convective system in the tropics. *J. Atmos. Sci.,* **40,** 1835–1850.

Goodman, S. J., and D. R. MacGorman, 1986: Cloud-to-ground lightning activity in mesoscale convective complexes. *Mon. Wea. Rev.,* **114,** 2320–2328.

Griffith, C. G., 1987: Comparisons of gauge and satellite rain estimates for the central United States during August 1979. *J. Geophys. Res.,* **92,** 9551–9566.

Houze, R. A., Jr., 1977: Structure and dynamics of a tropical squall-line system. *Mon. Wea. Rev.,* **105,** 1540–1567.

——, and E. N. Rappaport, 1984: Air motions and precipitation structure of an early summer squall line over the eastern tropical Atlantic. *J. Atmos. Sci.,* **41,** 553–574.

Kane, R. J., Jr., C. R. Chelius and J. M. Fritsch, 1987: Precipitation characteristics of mesoscale convective weather systems. *J. Climate Appl. Meteor.,* **26,** 1345–1357.

Kincer, J. B., 1916: Daytime and nighttime precipitation and their economic significance. *Mon. Wea. Rev.,* **44,** 628–633.

Leary, C. A., 1984: Precipitation structure of the cloud clusters in a tropical easterly wave. *Mon. Wea. Rev.,* **112,** 313–325.

——, and E. N. Rappaport, 1987: The life cycle and internal structure of a mesoscale convective complex. *Mon. Wea. Rev.,* **115,** 1503–1527.

Maddox, R. A., 1980: Mesoscale convective complexes. *Bull. Amer. Meteor. Soc.,* **61,** 1374–1387.

——, 1981: The structure and lifecycle of midlatitude mesoscale convective complexes. Atmos. Sci. Pap. 336, Ph.D. thesis, 311 pp. [Available from Dept. Atmos. Sci., Colo. State Univ., Ft. Collins, CO 80523.]

——, 1983: Large-scale meteorological conditions associated with midlatitude, mesoscale convective complexes. *Mon. Wea. Rev.,* **111,** 1475–1493.

——, C. F. Chappell and L. R. Hoxit, 1979: Synoptic and meso-α scale aspects of flash flood events. *Bull. Amer. Meteor. Soc.,* **60,** 115–123.

——, K. W. Howard, D. L. Bartels and D. M. Rodgers, 1986: Mesoscale convective complexes in the middle latitudes. *Mesoscale Meteorology and Forecasting,* P. S. Ray, Ed., Amer. Meteor. Soc., 390–413.

McAnelly, R. L., and W. R. Cotton, 1986: Meso-β-scale characteristics of an episode of meso-α-scale convective complexes. *Mon. Wea. Rev.,* **114,** 1740–1770.

Means, L. L., 1944: The nocturnal maximum occurrence of thunderstorms in the midwestern states. Dept. of Meteor., University of Chicago Misc. Rep. 16, 37 pp.

Merritt, J. H., and J. M. Fritsch, 1984: On the movement of the heavy precipitation areas of mid-latitude mesoscale convective complexes. Preprints, *Tenth Conf. on Wea. Forecasting and Analysis,* Amer. Meteor. Soc., Clearwater Beach, 529–536.

Negri, A. J., R. F. Adler and P. J. Wetzel, 1984: Rain estimation from satellites: An examination of the Griffith-Woodley technique. *J. Climate Appl. Meteor.,* **23,** 102–116.

Panofsky, H. A., and G. W. Brier, 1968: *Some Applications of Statistics to Meteorology.* Pennsylvania State University, 224 pp.

Riley, G. T., M. G. Landin and L. F. Bosart, 1987: The diurnal variability of precipitation across the Central Rockies and adjacent Great Plains. *Mon. Wea. Rev.,* **115,** 1161–1172.

Rockwood, A. A., D. L. Bartels and R. A. Maddox, 1984: Precipitation characteristics of a dual mesoscale convective complex. NOAA Tech. Memo. ERL ESG-6, U.S. Dept. Commerce, National Oceanic and Atmospheric Administration, Environmental Research Laboratories, Environmental Sciences Group, Boulder, CO 80303, 50 pp.

Rodgers, D. M., M. J. Magnano and J. H. Arns, 1985: Mesoscale convective complexes over the United States during 1983. *Mon. Wea. Rev.,* **113,** 888–901.

Rutledge, S. A., R. A. Houze, Jr., M. I. Biggerstaff and T. Matejka, 1988: The Oklahoma-Kansas mesoscale convective system of 10–11 June 1985: Precipitation structure and single-doppler radar analysis. *Mon. Wea. Rev.,* **116,** 1409–1430.

——, and D. R. MacGorman, 1988: Cloud-to-ground lightning activity in the 10–11 June 1985 mesoscale convective system observed during Oklahoma-Kansas PRE-STORM project. *Mon. Wea. Rev.,* **116,** 1393–1408.

Scofield, R. A., 1987: The NESDIS operational convective precipitation estimation technique. *Mon. Wea. Rev.,* **115,** 1773–1792.

Smull, B. F., and R. A. Houze, Jr., 1985: A midlatitude squall line with a trailing region of stratiform rain: Radar and satellite observations. *Mon. Wea. Rev.,* **113,** 117–133.

U.S. Weather Bureau and U.S. Corps of Engineers, 1947: *Thunderstorm Rainfall.* Hydrometeor. Rep. 5, Parts 1 and 2. Waterways Experiment Station, Vicksburg, MS [U.S. Government Document C30.44:5], 671 pp.

Wallace, J. M., 1975: Diurnal variations in precipitation and thunderstorm frequency over the conterminous United States. *Mon. Wea. Rev.,* **103,** 406–419.

Watson, A. I., J. G. Meitín and J. B. Cunning, 1988: Evolution of the kinematic structure and precipitation characteristics of a mesoscale convective system on 20 May 1979. *Mon. Wea. Rev.,* **116,** 1555–1567.

Wetzel, P. J., W. R. Cotton and R. L. McAnelly, 1983: A long-lived mesoscale convective complex. Part II: Evolution and structure of the mature complex. *Mon. Wea. Rev.,* **111,** 1919–1937.

Winkler, J. A., B. R. Skeeter and P. D. Yamamoto, 1988: Seasonal variations in the diurnal characteristics of heavy hourly precipitation across the United States. *Mon. Wea. Rev.,* **116,** 1641–1658.

Zipser, E. J., 1977: Mesoscale and convective-scale downdrafts as distinct components of squall-line structure. *Mon. Wea. Rev.,* **105,** 1568–1589.

——, 1982: Use of a conceptual model of the life-cycle of mesoscale convective systems to improve very-short-range forecasts. *Nowcasting,* K. A. Browning, Ed., Academic Press, 191–204.